TOWARDS MULTI-SCALE REACTING FLUID-STRUCTURE INTERACTION: MICRO-SCALE STRUCTURAL MODELING

A Thesis
Presented to
The Academic Faculty

by

Timothy Gallagher

In Partial Fulfillment
of the Requirements for the Degree
Master of Science in the
School of Aerospace Engineering

Georgia Institute of Technology
May 2015

TOWARDS MULTI-SCALE REACTING FLUID-STRUCTURE INTERACTION: MICRO-SCALE STRUCTURAL MODELING

Approved by:

Dr. Suresh Menon, Advisor
School of Aerospace Engineering
Georgia Institute of Technology

Dr. Julian Rimoli
School of Aerospace Engineering
Georgia Institute of Technology

Dr. Wenting Sun
School of Aerospace Engineering
Georgia Institute of Technology

Date Approved: November 5, 2014

TABLE OF CONTENTS

LIST OF TABLES

LIST OF FIGURES

SUMMARY

The fluid-structure interaction of reacting materials requires computational models capable of resolving the wide range of scales present in both the condensed phase energetic materials and the turbulent reacting gas phase. This effort is focused on the development of a micro-scale structural model designed to simulate heterogeneous energetic materials used for solid propellants and explosives. These two applications require a model that can track moving surfaces as the material burns, handle spontaneous formation of discontinuities such as cracks, model viscoelastic and viscoplastic materials, include finite-rate kinetics, and resolve both micro-scale features and macro-scale trends. Although a large set of computational models is applied to energetic materials, none meet all of these criteria. The Micro-Scale Dynamical Model serves as the basis for this work. The model is extended to add the capabilities required for energetic materials. Heterogeneous solid propellant burning simulations match experimental burn rate data and descriptions of material surface. Simulations of realistic heterogeneous plastic-bound explosives undergoing impact predict the formation of regions of localized heating called hotspots which may lead to detonation in the material. The location and intensity of these hotspots is found to vary with the material properties of the energetic crystal and binder and with the impact velocity. A statistical model of the hotspot peak temperatures for two frequently used energetic crystals indicates a linear relationship between the hotspot intensity and the impact velocity. This statistical model may be used to generate hotspot fields in macro-scale simulations incapable of resolving the micro-scale heating that occurs in heterogeneous explosives.

CHAPTER I

INTRODUCTION

1.1 Motivation

Energetic materials are solids or liquids containing large quantities of chemical energy. Solid energetic materials are typically composed of explosive crystals mixed into a soft binding material. This heterogeneous mixture is called a plastic- or polymer-bound explosive (PBX). The binder material allows the energetic material to be shaped arbitrarily while also absorbing and dissipating the mechanical energy imparted to the material during impacts. Energetic materials release their stored chemical energy through both deflagration and detonation processes.

Deflagration is the primary energy release mechanism for the solid propellants used in rocket motors. The micro-scale fluctuations in the propellant burning may couple with the large-scale flow characteristics to affect the global stability of the combustion process [4]. On the other hand, detonation is the primary mechanism of energy release in the explosives used for mining and weaponry. Detonation may occur intentionally or unintentionally during the manufacturing or transport of the energetic materials. Understanding the mechanisms by which energetic materials detonate is critical for the safe use, transport, and storage of the materials.

Numerical simulations provide a safe means to study both the deflagration and detonation of energetic materials. A computational model applied to the surface burning of solid propellants must be able to resolve the micro-scale fluctuations in the instantaneous burn rates that occur due to the interactions with the global flow. Meanwhile, models used to study the detonation initiation process need to resolve

the localized heating in the material due to the stresses induced by impacts. To address both of these applications, a computational model should have several features to render it robust and capable of predicting the performance and stability of energetic materials. The physical capabilities critical to simulating energetic material deflagration and detonation are:

1. Explicit tracking of surface regression due to pyrolysis and surface deformation due to impact loading.

2. Formation of discontinuities such as cracks and plasticizer debonding at arbitrary locations and times not known *a priori*;

3. Ability to model viscoelastic and viscoplastic materials;

4. Inclusion of finite-rate chemical kinetics;

5. Resolution of physical processes at scales approaching the micrometer length scales typical of hotspot formation and energetic crystal sizes;

6. Resolution of macro-scale physical processes such as global burn rates and macro-scale surface deformation.

In this work, an existing computational model which addresses most of the aforementioned points is extended to add the missing capabilities. This creates a structural solver that is capable of simulating the surface features important in deflagration and also is capable of simulating the processes leading up to detonation in energetic materials. The ability to couple the structural solver with a fluid solver is critical to the future success of this model. The actual coupling with a fluid solver is outside of the scope of this work; however, it is a motivating factor in the design of the solver.

1.2 Computational Models for Energetic Materials

There are several computational approaches in use to simulate energetic materials with the most common approaches presented below and discussed in light of the desired capabilities listed above. The methods are in increasing order of their spatial and temporal resolution, starting with the atomistic approaches. No single method from those surveyed addresses all of the capabilities desired. The deficiencies in the existing models is the primary motivator for the proposed computational model.

At the smallest scales, Molecular Dynamics (MD) approaches simulate the interactions between the atoms in a material. These interactions are defined by empirically derived interaction potentials (classical MD) or interaction potentials determined from quantum mechanics (Quantum Molecular Dynamics, or QMD). Simulations may be comprised of billions of atoms, but computational limitations prevent these methods from simulating systems larger than tens of nanometers for longer than a few picoseconds [2, 39]. The Dissipative Particle Dynamics (DPD) method is designed to overcome these length and time constraints. Instead of simulating the interactions of individual atoms, each node represents a molecule or a small discrete volume of material. While successful at relaxing the length and time scale restrictions of MD simulations, DPD simulations have an upper bound of microns and microsecond space and time scales [25, 44].

Continuum methods become usable at the micron length scale and larger. Finite volume, finite difference, and finite element methods are frequently used for simulating energetic materials. The representation of heterogeneous materials requires the solution of an additional levelset equation, typically resulting in a diffusion of the material interface over several computational cells [34, 60]. Additionally, because such methods are based on the differential form of the governing equations, discontinuities due to fractures and debonding are difficult to treat [55].

Continuum Lagrangian approaches such as Smoothed Particle Hydrodynamics

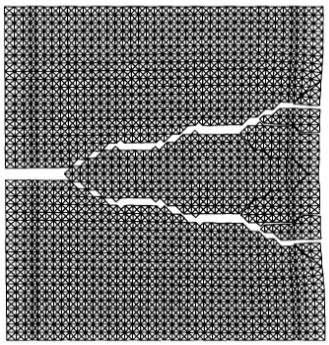

(a) Example of crack formation between elements (from [61])

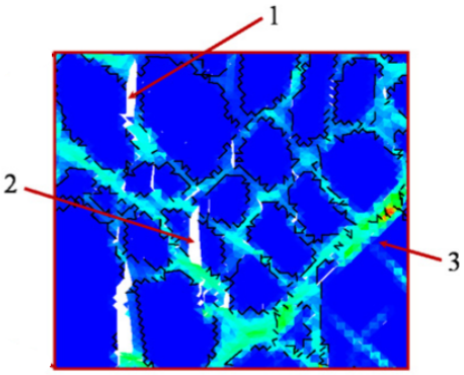

(b) PBX simulation of 1) debonding, 2) fracture and 3) localized heating (from [7])

Figure 1: Examples from CFEM simulations.

(SPH) allow the deforming surface of the energetic material to be tracked explicitly without additional equations. The interfaces between materials are also straightforward to model with each Lagrangian particle representing a single material. Each particle is updated by integrating the continuum partial differential equation weighted by a kernel function on a support domain. The definition of the support domain requires finding the nearest neighboring particles, adding to the expense of the method. Like the Eulerian approaches, special treatment is required in the presence of discontinuities [42].

The Cohesive Finite Element Method (CFEM) is close to meeting all of the requirements in a model. CFEM uses a traditional finite element discretization combined with a cohesive traction element on the surfaces between the traditional elements. The traction forces between the elements are designed to model the friction as elements slide past one another as well as the normal forces required to separate elements [61]. This allows both spontaneous crack formation and material debonding as shown in Figure 1. Unfortunately, discontinuities may only form along cohesive surfaces which requires either *a priori* knowledge of the discontinuity locations or placing cohesive surfaces between all elements.

This cross-section of computational techniques reveals that there are a wide variety of methods but no one method has all of the desired features. In particular, the ability to predict spontaneous discontinuity formation without special treatment requires an approach that does not rely on the differential form of the governing equations. This, along with the ability to resolve micron-sized imperfections in materials, is the primary motivation behind the Micro-Scale Dynamical Model (MSDM) proposed by Li *et al* for the erosion of materials used in industrial applications [39]. The ability to handle spontaneous discontinuities is also the primary motivation behind the peridynamic theory introduced by Silling in 2000 [55] and described in the next section.

MSDM uses a lattice of Lagrangian masses connected to their nearest neighbors by springs [39]. The original model meets most of the requirements given previously:

1. *Explicit surface tracking.*

   As a Lagrangian method, the surface deformation or regression is explicitly tracked as the convex hull of the Lagrangian nodes.

2. *Formation of discontinuities.*

   By allowing the springs to break when the strain between sites exceeds the fracture strain of the materials, discontinuities may form at any point in the lattice without *a priori* knowledge of the fracture locations.

3. *Viscoelastic and viscoplastic materials.*

   Omitted in the original model, dampers may be added, in addition to the springs, between sites to allow for strain-rate dependent effects when needed. These can be combined in a variety of ways to represent Maxwell materials, Kelvin-Voigt materials, or Standard Linear materials. Plastic effects may also be included by tracking the accumulated strain of each connection and modifying the Young's Modulus to approximate the stress-strain relation as a series

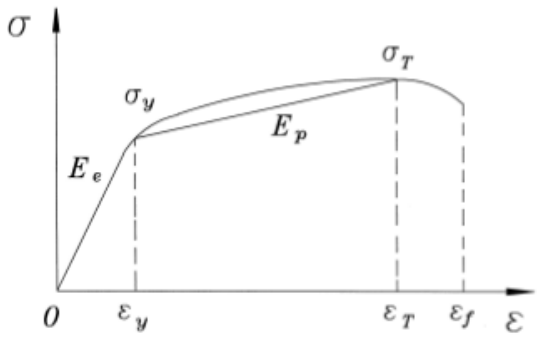

Figure 2: Linear approximations used in MSDM for plastic effects. Accuracy improves by increasing the number of linear segments in the plastic regime (from [39])

of constant-slope sections as shown in Figure 2.

4. *Finite-rate kinetics.*

   The original MSDM formulation does not include an energy equation prohibiting the use of finite-rate kinetics. This effort extends the model to include an energy equation.

5. *Resolution on the micron scale.*

   The original motivation outlined in Li *et al* is to bridge the scales between molecular dynamics and the large-scale behavior of materials by resolving the material at the micro-scale [39].

6. *Resolution of macro-scale.*

   The purpose of the model is to determine the erosive wear, a macro-scale effect, of materials due to micro-scale effects. The model has been used to study composite materials [14], corrosion of reactive materials resulting in weakening of the inter-node bonds [15], porous materials [38], and the corrosion of non-reactive materials [40].

Based on the list of desired features for a structural solver, the original MSDM formulation meets all but a few of the requirements. In this work, the method is

extended to include the missing features. Additionally, MSDM is shown to be a peridynamic approach to continuum mechanics. This link to peridynamics is important; the original MSDM formulation is presented without a theoretical proof that the method converges to classical continuum mechanics governed by the differential form of the governing equations. Silling and Lehoucq demonstrate the convergence to classical elastic theory [57] while Seleson *et al* [52] and Lehoucq and Silling [37] both verify the convergence at the micro-scale to molecular dynamics. The theoretical justification for MSDM as a continuum model bridging the scales from micro- to macro-scales is provided by demonstrating MSDM fits within the peridynamic theory. The details of the MSDM formulation and the link to peridynamics are given in Chapter 2.

1.3 Peridynamic Theory

The following is a description of the peridynamic theory for solid mechanics. Only the important descriptions and conclusions of the theory are summarized here. Readers interested in the associated proofs are directed to the work by Silling [55].

In the peridynamic theory, the acceleration of a point is determined by the force density which is a function of the displacement field $\boldsymbol{d}$ in the neighborhood $\mathcal{R}$ around its position $\boldsymbol{x}$:

$$\rho\ddot{\boldsymbol{d}} = \int_{\mathcal{R}} \boldsymbol{f}(\boldsymbol{d}(\boldsymbol{x}',t) - \boldsymbol{d}(\boldsymbol{x},t), \boldsymbol{x}' - \boldsymbol{x}) dV_{x'} + \boldsymbol{b} \tag{1}$$

and $\boldsymbol{b}$ is a body force density, $\boldsymbol{f}$ is a pairwise force function and ρ is the density. The neighborhood $\mathcal{R}$ is composed of all the coordinates within the force horizon δ centered around $\boldsymbol{x}$. Taking $\boldsymbol{\xi} = \boldsymbol{x}' - \boldsymbol{x}$ as the relative position of two points in the reference configuration and $\boldsymbol{\eta} = \boldsymbol{d}(\boldsymbol{x}',t) - \boldsymbol{d}(\boldsymbol{x},t)$ as the difference in displacements for the two points, the relative position of the particles in the deformed configuration is $\boldsymbol{\eta} + \boldsymbol{\xi}$. This is illustrated in Figure 3. With these definitions, the force function becomes $\boldsymbol{f}(\boldsymbol{d}(\boldsymbol{x}',t) - \boldsymbol{d}(\boldsymbol{x},t), \boldsymbol{x}' - \boldsymbol{x}) = \boldsymbol{f}(\boldsymbol{\eta}, \boldsymbol{\xi})$.

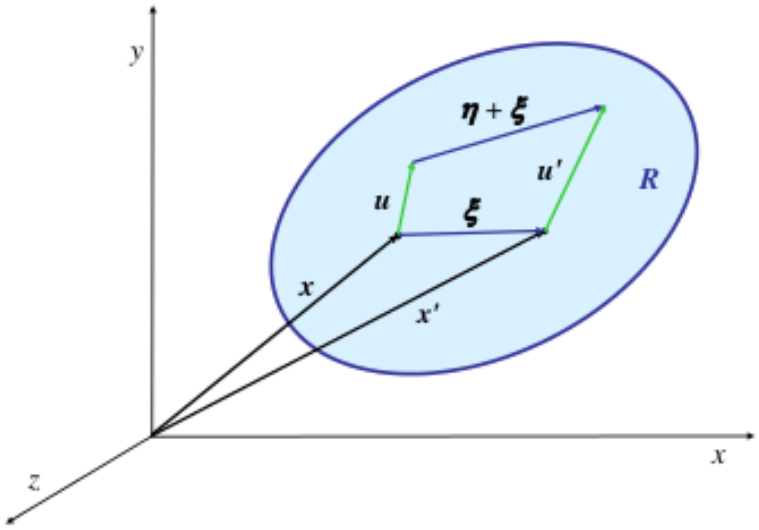

Figure 3: Representation of the position vectors defined in the peridynamic formulation (from [18])

The choice of the force function is not arbitrary. The force functions must satisfy Newton's third law:

$$\boldsymbol{f}(-\boldsymbol{\eta}, -\boldsymbol{\xi}) = -\boldsymbol{f}(\boldsymbol{\eta}, \boldsymbol{\xi}); \qquad \forall \boldsymbol{\eta}, \boldsymbol{\xi} \tag{2}$$

which is called the *linear admissibility* of the force function. Additionally, conservation of angular momentum requires:

$$(\boldsymbol{\xi} + \boldsymbol{\eta}) \times \boldsymbol{f}(\boldsymbol{\eta}, \boldsymbol{\xi}) = 0; \qquad \forall \boldsymbol{\eta}, \boldsymbol{\xi} \tag{3}$$

which is the *angular admissibility* of the force function. The angular admissibility requirement states that the force pairs are directed along the vector $\boldsymbol{\xi}$. A general form of the force function that satisfies both Equations 2 and 3 is:

$$\boldsymbol{f}(\boldsymbol{\eta}, \boldsymbol{\xi}) = F(\boldsymbol{\eta}, \boldsymbol{\xi})(\boldsymbol{\eta} + \boldsymbol{\xi}); \qquad \forall \boldsymbol{\eta}, \boldsymbol{\xi} \tag{4}$$

where F is a scalar function. Chapter 2 demonstrates the link between MSDM and peridynamics.

1.4 Heterogeneous Solid Propellant Burning

For over 70 years numerous scientists studied the combustion of the heterogeneous solid propellants used in solid rocket motors. The most commonly used propellant is composed of the salt Ammonium Perchlorate (AP) mixed with the Hydroxl-Terminated Polybutadiene binder (HTPB). Early studies focused on either the chemical decomposition over a range of pressures or on the detailed surface structure of the propellant. The 1969 review article by Jacobs and Whitehead [30] combined 15 years of research into the chemical decomposition and combustion of AP. The detailed reaction mechanisms are split into low and high temperature combustion regimes, combustion in the presence of additives or catalysts and the detonation of AP.

Similarly, in a series of experiments Boggs identified four combustion regimes based on the ambient pressure of a nitrogen atmosphere [12]. Figure 4 breaks the AP combustion regime into these regions. The first regime is characterized by steady, planar regression in the single crystal with the liquid layer and gaseous products producing a frothy or foam layer. As pressure increases, the thickness of this foam layer decreases. The second regime is macroscopically planar but closer inspection reveals ridges and valleys. The foam layer is no longer present and the reaction progresses directly from the solid to gaseous phases. This direct transfer results in a close coupling between gas and solid phases. In the present effort, the simulation of surface burning will be confined to the upper end of the first regime through the entirety of the second regime. The model used is confined only to the solid phase and this regime is chosen to avoid the need for a liquid phase at the interface layer.

With the wealth of experimental data and early, rudimentary analytical models, Beckstead, Derr and Price proposed a predictive model for AP-HTPB combustion [11]. The BDP model postulates a triple flame structure over each AP crystal in the propellant. A laminar AP monopropellant flame sits just above the crystal. A diffusion flame resides between the gaseous AP and the gaseous binder and is

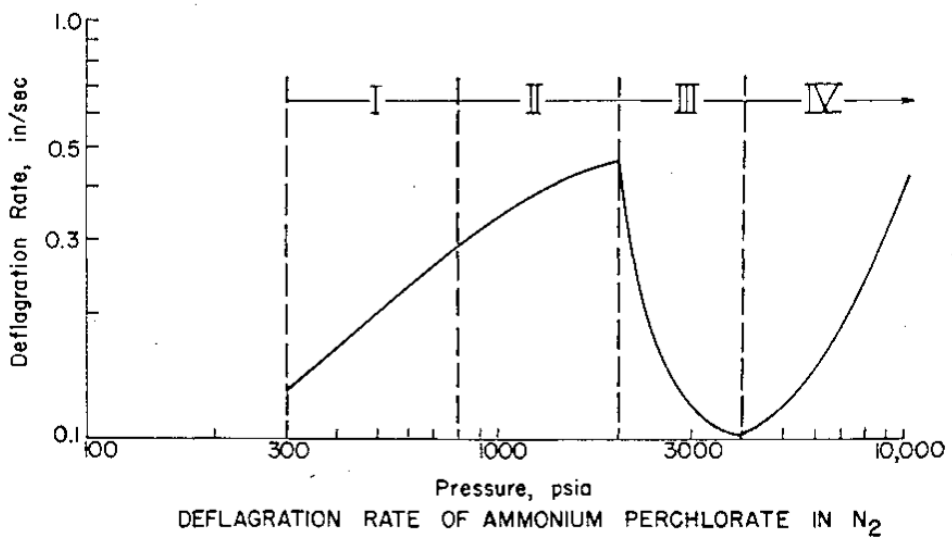

Figure 4: Four combustion regimes of AP depending on the ambient pressure (from [12])

designated as the primary flame. Lastly, there is a diffusion flame sitting above the primary flame between the oxygen-rich AP monopropellant products and the fuel-rich binder decomposition products. Figure 5 is a sketch of the BDP flame structure. The BDP model predicts the surface temperature over the heterogeneous propellant can be treated as uniform and depends on the standoff distance of the primary flame. As the ambient pressure increases, the primary flame is pushed closer to the surface resulting in a higher surface temperature [11]. Despite improvements to the BDP model such as the Cohen-Strand model [16], the BDP model serves as the baseline for modern work [21].

Frazier, Demko and Petersen recently extended the BDP model to include catalytic nanoparticle additives [21]. Numerical results are compared to experimental results for several of AP-HTPB propellants with varying amounts and sizes of the AP particles. The authors report little sensitivity in the binder reaction rates when the nanoparticles are present. Therefore, an empirical constant that only modifies the reaction rate of the AP reaction when nanoparticles are present is given. The model

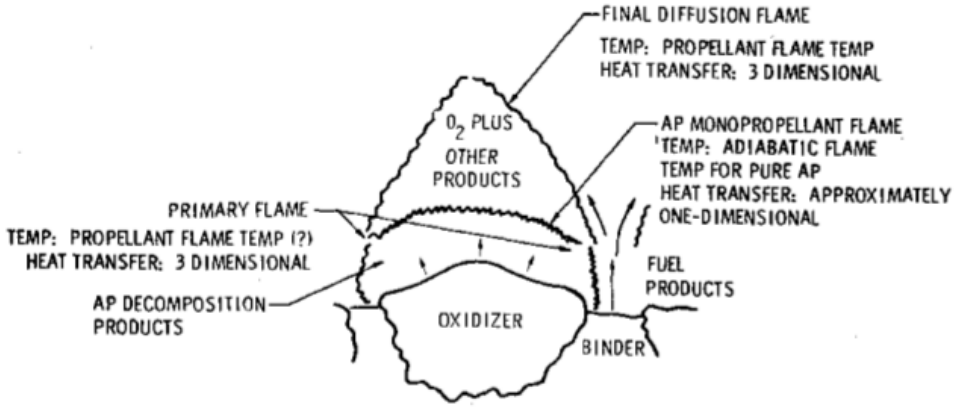

Figure 5: Beckstead-Derr-Price flame model for AP-HTPB heterogeneous combustion (from [11])

used by Frazier, Demko and Petersen is 1D and unable to provide any information about the surface structure. The results of the extended model and experiments serve as the baseline for evaluating the capability of MSDM to simulate heterogeneous solid propellant combustion.

1.5 Hotspot Formation in Heterogeneous Explosives

Researchers discovered in the 1940s that localized regions of high temperature in energetic materials initiates detonation of the material. These early experiments were performed on liquid explosives as a means to systematically determine the impact sensitivity of the materials [50]. Some explosives are sensitive to even the mildest agitation while others require considerable thermal or mechanical energy to detonate. Understanding the hotspot formation process is a key to safe handling of energetic materials.

In the initial experiments on liquid explosives, the researchers noted that the impact sensitivity was greatly increased by the addition of tiny gas bubbles in the liquid. It was postulated that the adiabatic heating from the compression of the gas bubbles created the hotspots that triggered the detonation [50]. Bubble like

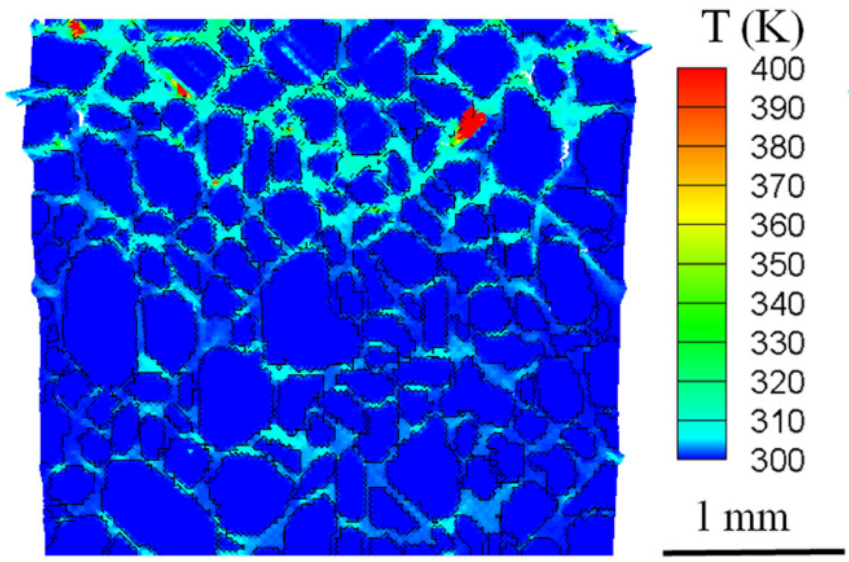

Figure 6: Temperature distribution showing hotspots in a digitized image of a real PBX (from [7])

.

structures called pores or voids may also appear in solids where the heating due to adiabatic compression is augmented by the viscoplastic work done as the void collapses. Numerical simulations performed by Tran and Udaykumar [58, 59] reveal the different mechanisms of void collapse and the conversion of the mechanical energy into heat.

In addition to void collapse, material inhomogeneities also generate localized heating which may be strong enough to trigger detonations. Barua and Zhou [7] used the Cohesive Finite Element Method to study the hotspot formation in PBXs underging impact. The strain rate due to impact, the lateral confinement and the energetic crystal packing densities were varied. Figure 6 shows the temperature in the PBX undergoing strain as computed by Barua and Zhou [7]. The hotspots form in the binder material and transfer heat to the energetic crystals. Therefore, the binder properties are strongly correlated to hotspot formation.

An energy budget based on the contributions of the terms in the energy equation reveal that viscoelastic work is the primary cause of hotspot formation at early times.

At later times, the formation of cracks and friction along the crack surfaces contributes more to the heating. At low strain rates or for soft binders, the hotspots occur primarily along shear bands and are distributed throughout the energetic material. At larger strain rates or for harder binders, the hotspots are more localized to the impact face [7]. The work of Barua and Zhou serves as the basis for evaluating MSDM's capability to study the hotspot formation processes in energetic materials.

1.6 Objectives

The following key objectives and associated tasks will establish and demonstrate MSDM is a structural solver capable of studying energetic materials:

1. **Extend and validate MSDM for energetic materials.**

   The simulation of both the deflagration of heterogeneous solid propellants and the hotspot formation in plastic bound explosives requires a computational model that meets six primary criteria:

   (a) Explicit tracking of surface regression due to pyrolysis and surface deformation due to impact loading;

   (b) Formation of discontinuities such as cracks and plasticizer debonding at arbitrary locations and times not known *a priori*;

   (c) Ability to model viscoelastic and viscoplastic materials;

   (d) Inclusion of finite-rate chemical kinetics;

   (e) Resolution of physical processes at scales approaching the micrometer length scales typical of hotspot formation and energetic crystal sizes;

   (f) Resolution of macro-scale physical processes such as global burn rates and macro-scale surface deformation.

   Several existing computational models are surveyed and although each addresses a subset of the criteria, none of the commonly used models addresses them all.

The original MSDM formulation meets all of the criteria except the inclusion of finite-rate chemical kinetics and the ability to model viscoelastic or viscoplastic materials. The original model includes plastic deformation but does not include viscous effects. Extensions to MSDM will be performed to enable the simulation of heterogeneous solid propellant combustion and hotspot formation in energetic materials.

2. **Demonstrate MSDM is capable of simulating heterogeneous solid propellant combustion.**

   The global stability of solid rocket motors may be coupled to the combustion characteristics of the solid propellant grain [3]. The combustion characteristics of solid propellants depends on:

   (a) The unsteady mass flux and energy release from the propellant;

   (b) Resolution of the detailed surface structure at a microscopic level.

   MSDM will be evaluated on its ability to resolve these two features of propellant combustion.

3. **Apply MSDM to the prediction of hotspot formation in plastic bound explosives.**

   The detonation of plastic bound explosives may be intentionally triggered through impact or shock or it may be unintentionally triggered by impacts during the manufacturing, transport, or storage of the material. The detonation process is initiated by localized regions of high temperature called hotspots. Understanding the mechanisms of hotspot formation from impacts is critically important for the safe handling of energetic materials. The important factors in hotspot formation are:

   (a) Binder material properties;

(b) Energetic crystal material properties;

(c) Energetic crystal packing density;

(d) Impact velocity.

MSDM will be used to capture the hotspot formation in energetic materials due to impact under a variety of conditions.

CHAPTER II

MODEL FORMULATION

2.1 Discrete Lattice Formulation

A material is modeled as a discrete lattice of Lagrangian masses connected via springs and/or dampers. The structured connections eliminate the need for costly nearest neighbor searches because the connections are determined during the problem setup and are based on lattice indexing. Internal and surface nodes and their connections are demonstrated in Figure 7. The boundary nodes of the material have an additional layer of ghost nodes attached for the application of boundary conditions. These exterior nodes can be considered another solid, a fluid, or a communication node. A node along the surface of a solid material exposed to a fluid is demonstrated in Figure 7b. Each node represents the homogenized material contained within the volume of the dual-mesh which is computed only within the solid portion of the grid. Figure 8 demonstrates the dual-mesh for different configurations around the central node where the dashed lines indicate the homogenized volume.

The lattice nodes are connected to those around them by springs with the potential for multiple springs and dampers in series and/or parallel if needed to model materials that exhibit visco/hyperplastic or visco/hyperelastic behavior [17, 20]. Springs connecting nodes diagonal from each other may be added to accurately capture shear behavior [10]. In the original formulation, the effective spring constant is defined as $k = E|\boldsymbol{l_0}(\boldsymbol{x}, \boldsymbol{x}', t)|$ where E is the Young's Modulus and $\boldsymbol{l_0}(\boldsymbol{x}, \boldsymbol{x}', t)$ is the direction vector in the undeformed state from the node at $\boldsymbol{x}$ to the node at $\boldsymbol{x}'$. This vector is, in general, a function of time when plastic effects are included. The resulting force on the node, including hysteretic and viscous damping (with damping coefficients μ

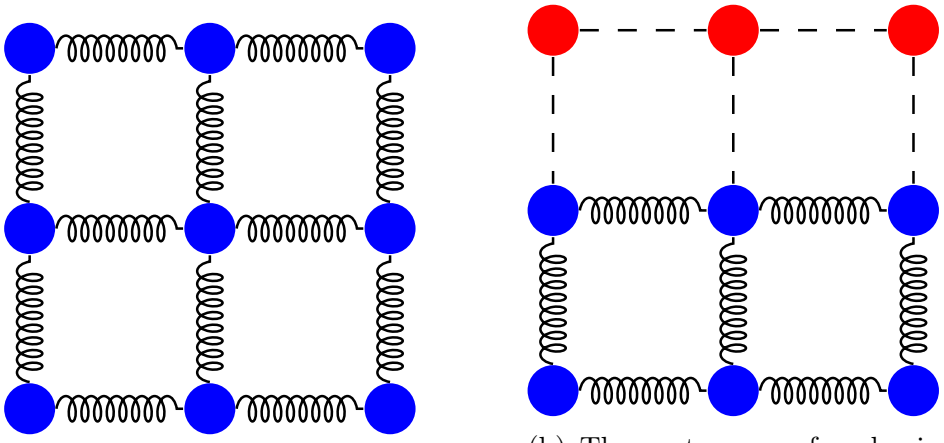

(a) The center node is entirely surrounded by solid nodes

(b) The center row of nodes is exposed to fluid on the top side; no springs connect the fluid nodes to the solid nodes

Figure 7: Demonstration of lattice nodes; blue nodes indicate solid (interior) nodes while red nodes indicate fluid (exterior) nodes.

and c respectively and $i = \sqrt{-1}$), is thus [40]:

$$\begin{aligned}
\boldsymbol{f}(\boldsymbol{x}, \boldsymbol{x}', t) &= (k + i\mu)\left[d(\boldsymbol{x}', t) - d(\boldsymbol{x}, t) - \boldsymbol{l_0}(\boldsymbol{x}, \boldsymbol{x}', t)\right] \\
&\quad + c\frac{D}{Dt}\left[d(\boldsymbol{x}', t) - d(\boldsymbol{x}, t) - \boldsymbol{l_0}(\boldsymbol{x}, \boldsymbol{x}', t)\right] \\
&= \left(E\left|\boldsymbol{l_0}(\boldsymbol{x}, \boldsymbol{x}', t)\right| + i\mu\right)\left[d(\boldsymbol{x}', t) - d(\boldsymbol{x}, t) - \boldsymbol{l_0}(\boldsymbol{x}, \boldsymbol{x}', t)\right] \\
&\quad + c\frac{D}{Dt}\left[d(\boldsymbol{x}', t) - d(\boldsymbol{x}, t) - \boldsymbol{l_0}(\boldsymbol{x}, \boldsymbol{x}', t)\right]
\end{aligned} \tag{5}$$

Recalling the definition of $\boldsymbol{\eta}$ and recognizing that $\boldsymbol{l_0}(\boldsymbol{x}, \boldsymbol{x}') = -\boldsymbol{\xi}$, Equation 5 is recast:

$$\begin{aligned}
\boldsymbol{f}(\boldsymbol{\eta}, \boldsymbol{\xi}, t) &= \left(E\left|\boldsymbol{\xi}\right| + i\mu\right)\left[\boldsymbol{\eta} + \boldsymbol{\xi}\right] + c\frac{D}{Dt}\left[\boldsymbol{\eta} + \boldsymbol{\xi}\right] \\
&= \left(E\left|\boldsymbol{\xi}\right| + i\mu + c\frac{D}{Dt}\right)\left[\boldsymbol{\eta} + \boldsymbol{\xi}\right] \\
&= F(\boldsymbol{\eta}, \boldsymbol{\xi})\left[\boldsymbol{\eta} + \boldsymbol{\xi}\right]
\end{aligned} \tag{6}$$

where now Equation 6 is in a form identical to Equation 4 where F is a scalar operator and not a scalar function. It is trivial to show that the linear admissibility requirement, Equation 2 holds.

It remains to show that the scalar operator F derived for pairwise forces including both hysteretic and viscous damping in Equation 6 satisfies the angular admissibility

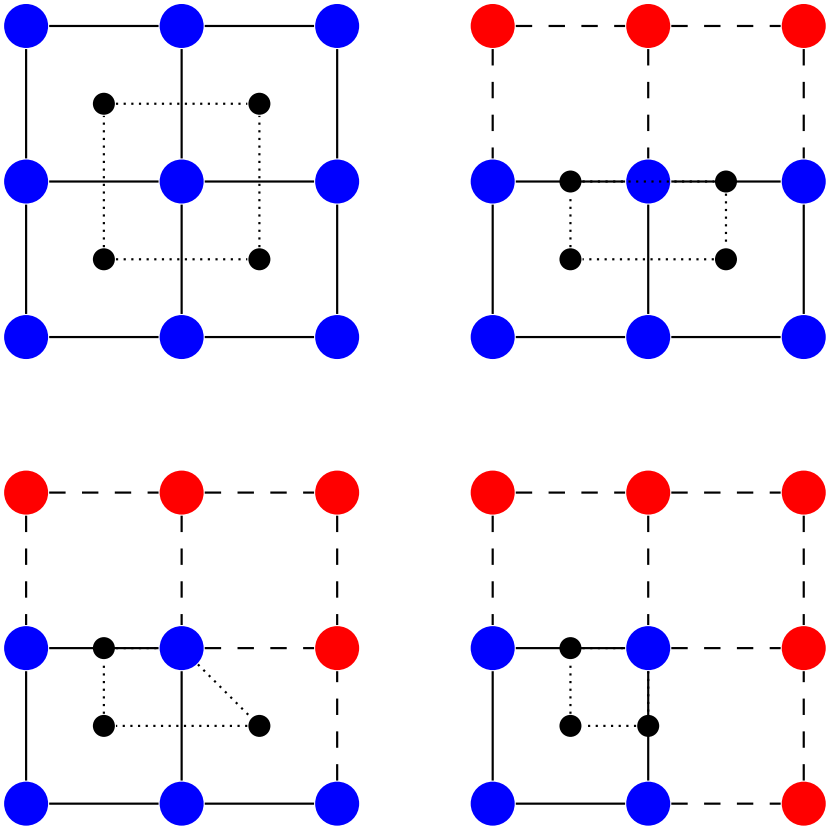

Figure 8: Dual-mesh used to compute the volume of the central solid node in the lattice. The solid nodes are indicated by blue nodes while boundary nodes not contributing to the volume are indicated by red nodes; the black nodes are the locations of the dual-mesh.

requirement in Equation 3.

Substituting Equation 6 into Equation 3 and using the distributive property and scalar multiplication property of the cross product yields:

$$E\left|\boldsymbol{\xi}\right|\left(\boldsymbol{\xi}+\boldsymbol{\eta}\right)\times\left[\boldsymbol{\eta}+\boldsymbol{\xi}\right]+i\lambda\left(\boldsymbol{\xi}+\boldsymbol{\eta}\right)\times\left[\boldsymbol{\eta}+\boldsymbol{\xi}\right]+c\left(\boldsymbol{\xi}+\boldsymbol{\eta}\right)\times\left[\dot{\boldsymbol{\eta}}+\dot{\boldsymbol{\xi}}\right]=0$$

The first two terms related to the spring stiffness and hysteretic damping are zero. If there is no viscous damping such that $c=0$ then the angular admissibility is satisfied.

If $c\neq 0$:

$$\begin{aligned}\left(\boldsymbol{\xi}+\boldsymbol{\eta}\right)\times\left[\dot{\boldsymbol{\eta}}+\dot{\boldsymbol{\xi}}\right] &= 0\\ \Rightarrow\boldsymbol{\xi}\times\dot{\boldsymbol{\eta}}+\boldsymbol{\xi}\times\dot{\boldsymbol{\xi}}+\boldsymbol{\eta}\times\dot{\boldsymbol{\eta}}+\boldsymbol{\eta}\times\dot{\boldsymbol{\xi}} &= 0\end{aligned}$$

Using the chain rule for derivatives involving cross products:

$$\frac{d}{dt}\left(\boldsymbol{a}\times\boldsymbol{b}\right)=\frac{d\boldsymbol{a}}{dt}\times\boldsymbol{b}+\boldsymbol{a}\times\frac{d\boldsymbol{b}}{dt}$$

gives:

$$\begin{aligned}&\frac{d}{dt}\left(\boldsymbol{\xi}\times\boldsymbol{\eta}\right)-\dot{\boldsymbol{\xi}}\times\boldsymbol{\eta}-\dot{\boldsymbol{\xi}}\times\boldsymbol{\xi}-\dot{\boldsymbol{\eta}}\times\boldsymbol{\eta}+\frac{d}{dt}\left(\boldsymbol{\eta}\times\boldsymbol{\xi}\right)-\dot{\boldsymbol{\eta}}\times\boldsymbol{\xi}=0\\ \Rightarrow&-\dot{\boldsymbol{\xi}}\times\boldsymbol{\eta}-\dot{\boldsymbol{\xi}}\times\boldsymbol{\xi}-\dot{\boldsymbol{\eta}}\times\boldsymbol{\eta}-\dot{\boldsymbol{\eta}}\times\boldsymbol{\xi}=0\end{aligned}$$

Grouping the terms together, this becomes:

$$\left(\dot{\boldsymbol{\xi}}+\dot{\boldsymbol{\eta}}\right)\times\left(\boldsymbol{\xi}+\boldsymbol{\eta}\right)=0 \tag{7}$$

This result is simply the negative of the starting expression when $c\neq 0$ which means it is always true for any $\boldsymbol{\xi}$, $\boldsymbol{\eta}$, $\dot{\boldsymbol{\xi}}$, $\dot{\boldsymbol{\eta}}$. This is consistent with the cases without damping which require the displacement and force vectors to be aligned [55].

Finally, Equation 1 can be written:

$$\rho\ddot{\boldsymbol{d}}=\int_{\mathcal{R}}\boldsymbol{f}(\boldsymbol{\eta},\boldsymbol{\xi},t)\mu(\boldsymbol{x},\boldsymbol{x}')dV_{\boldsymbol{x}'} \tag{8}$$

where μ is an indicator function taking the value 1 if the two points are connected and 0 otherwise or if the bond has broken. With the discrete lattice, this integral becomes:

$$m\ddot{\boldsymbol{d}}=m\frac{D\boldsymbol{u}}{Dt}=\sum_{i=1}^{\text{neighbors}}\boldsymbol{f}(\boldsymbol{\eta}_i,\boldsymbol{\xi}_i,t) \tag{9}$$

where $\boldsymbol{u}$ is the particle velocity. The sum is computed only over the neighbors currently connected. This is identical to the approach used in meshfree peridynamic formulations except the indicator function is set at initialization and only changes due to fracture.

Therefore, this formulation is consistent with the *bond-based* peridynamic form. This means all of the constitutive information for the material is contained only in the pairwise bonds. The limitations of this model are [56]:

- The assumption that all forces are determined only by pairwise local conditions results in an effective Poisson's Ratio of 0.25 for homogeneous, isotropic materials;
- Plasticity may be included by deforming the pairwise bonds, but this erroneously results in permanent deformation under volumetric strain, inconsistent with experimental evidence that deformation occurs due to shear.

For the materials considered here, these limitations do not pose significant issues. The assumed Young's modulus is acceptable for the materials chosen and plastic effects are not considered.

2.2 Numerical Formulation

Each lattice node carries the solution vector $U = \{m_k, \boldsymbol{u}, V, P, T, e\}^T$ where m_k is the mass of the material component k in the volume ($\sum_k m_k = m =$ total mass), $\boldsymbol{u} = \dot{\boldsymbol{d}}$ is the velocity vector, V is the node volume, P is the pressure, T is the temperature, and $e = c_v T$ is the internal energy. The solution vector is evolved according to:

$$\frac{Dm_k}{Dt} = \dot{m}_k \tag{10a}$$

$$m\frac{D\boldsymbol{u}}{Dt} = \sum_{i=1}^{\text{parallel}} \left(\boldsymbol{f}_{\parallel i} + \boldsymbol{f}_{\perp i}\right) + \sum_{i=1}^{\text{diagonal}} \boldsymbol{f}_d + \boldsymbol{b} \tag{10b}$$

$$\frac{De}{Dt} = c_v \frac{dT}{dP}\frac{dP}{dt} + \sum_k h_k \dot{m}_k + \boldsymbol{\nabla} \cdot (k\boldsymbol{\nabla} T) \tag{10c}$$

where $\dot{m}_k$ is the consumption of mass of material k due to chemical reactions, c_v is the constant volume heat capacity, k is the thermal conductivity and h_k is the enthalpy of material k.

The momentum of the node is evolved using Newton's Second Law where the forces on the right-hand side of the equation are due to the springs and/or dampers connected between the nodes and any volumetric, or body, forces that operate on the node, $\boldsymbol{b}$. The nodes are connected along parallel sides of the element as shown previously in Figure 7. The forces that arise from these connections are $\boldsymbol{f}_{\parallel}$. More sophisticated connections are possible, a brief description is given in Chapter 5. These advanced models may introduce connections between diagonal nodes giving rise to forces $\boldsymbol{f_d}$. Some models introduce correction forces perpendicular to the forces which arise from the parallel connections [10]. These corrective forces are $\boldsymbol{f}_{\perp}$. Consistent with the previous MSDM works, diagonal springs, corrective forces, body forces and dampers are omitted in these simulations [14, 15, 29, 39, 40].

The physical regression (in units of length per time) due to chemical reactions is computed using Arrhenius rate equations derived from first principle simulations or experiments of pyrolysis rates. The details of this evolution and the connection to the mass consumption rate $\dot{m}_k$ is given in Sec. 2.4. The first two terms of the internal equation, Equation 10c, represent the heating (cooling) due to compression (expansion) and the heat released due to chemical reactions. The temperature flux is computed in a differential, rather than integral, fashion using second order centered finite differences along the connecting springs. Discontinuities due to fracture are

readily handled by ghost nodes taking the properties of the surrounding medium such that a heat flux from the material to the surrounding medium is computed.

The change in pressure dP/dt is computed using the change in volume, V, and the bulk modulus K:

$$\frac{dP}{dt} = -\frac{K dV/dt}{V} \tag{11}$$

The change in temperature with pressure is computed using an equation of state. The Mie-Gruneisen equation of state is used [64]:

$$P = \frac{\mathcal{G}}{\lambda}(e - e_0) + f(\lambda) \tag{12}$$

where:

$$f(\lambda) = P_{\mathcal{H}}\left[1 - \frac{\mathcal{G}}{2\lambda}(\lambda_0 - \lambda)\right] - \frac{\mathcal{G}}{2\lambda}P_0(\lambda_0 - \lambda) \tag{13a}$$

$$P_{\mathcal{H}} = P_0 + \frac{\rho_0 c_0^2 \phi}{(1 - s\phi)^2} \tag{13b}$$

$$\phi = 1 - \frac{\lambda}{\lambda_0} \tag{13c}$$

$$e = c_v T \tag{13d}$$

$$\lambda = \frac{1}{\rho} \tag{13e}$$

where $\mathcal{G}$ is the Gruneisen gamma, e_0 is the internal energy at the reference conditions (taken here to be $c_v T_0$ where $T_0 = 300K$), P_0 is the reference pressure (taken here to be 100 000 Pa), c_0 is the speed of sound at the reference conditions and s is the slope of the linear fit between shock velocity and particle velocity, $U_s = c_0 + s u_p$. This results in:

$$\frac{dT}{dP} = \frac{\lambda}{\mathcal{G}c_v} = \frac{V}{m\mathcal{G}c_v} \tag{14}$$

Substitution of Equations 11 and 14 into Equation 10c gives:

$$\frac{De}{Dt} = -\frac{K}{m\mathcal{G}c_v}\frac{dV}{dt} + \sum_k h_k \dot{m}_k + \boldsymbol{\nabla} \cdot (k \boldsymbol{\nabla} T) \tag{15}$$

The complete set of governing equations is thus defined by Equations 10a, 10b and 15.

2.3 Temporal Integration

The system of equations given by Equations 10a, 10b, and 15 may be solved by any numerical method suitable for ordinary differential equations. The class of methods used in this effort are in two categories: explicit schemes and implicit schemes. The explicit schemes are easy to implement but require very small time steps as the spring stiffness increases. The implicit schemes are more complicated to implement and involve the solution of a system of linear equations at each time step but allow significantly larger time steps. The cost of the linear system solver may be offset by the increased time step for large spring constants.

2.3.1 Explicit Schemes

Explicit schemes are simple to implement because they only depend on information already known from the current or previous values of the time integration. If the current time level is indicated with a superscript n, the next and previous levels by $n+1$ and $n-1$ respectively, the simplest explicit scheme may be written as:

$$\boldsymbol{u}^{n+1} = \boldsymbol{u}^n + \boldsymbol{a}^n \Delta t \tag{16}$$

where Δt is the increment in time and $\boldsymbol{a}$ is the acceleration. The position of the node is also updated explicitly:

$$\boldsymbol{x}^{n+1} = \boldsymbol{x}^n + \boldsymbol{u}^n \Delta t \tag{17}$$

This scheme is the Explicit Euler scheme and is first order accurate in time and the updated value of $\boldsymbol{u}$ depends only on known values of the velocity and the acceleration. For mass-spring systems, this scheme is numerically unstable without the addition of damping. However, it's simplicity and speed makes it a very popular choice in other applications of mass-spring systems such as computer graphics [5].

The Velocity-Verlet scheme is a popular choice for molecular dynamics and yields a second order accurate scheme [9]. It is based on the mid-point integration rule and can be shown to conserve energy, unlike the explicit Euler scheme:

$$\boldsymbol{x}^{n+1} = \boldsymbol{x}^n + \boldsymbol{v}^n \Delta t + \frac{1}{2}\boldsymbol{a}^n \Delta t^2 \tag{18a}$$

$$\boldsymbol{u}^{n+1} = \boldsymbol{u}^n + \frac{1}{2}\left(\boldsymbol{a}^n + \boldsymbol{a}^{n+1}\right)\Delta t \tag{18b}$$

2.3.2 Implicit Schemes

Implicit schemes allow relatively large time steps even for stiff systems. The simplest first order implicit scheme is the Implicit (or Backwards) Euler scheme:

$$\boldsymbol{u}^{n+1} = \boldsymbol{u}^n + \boldsymbol{a}^{n+1}\Delta t \tag{19}$$

In general, the acceleration at the next time step is unknown and depends on both the position and the velocity of the node at the next time step. The acceleration on the right hand side may be written more explicitly as $\boldsymbol{a}^{n+1} = \boldsymbol{M}^{-1}\boldsymbol{f}\left(\boldsymbol{x}^n + \Delta\boldsymbol{x}, \boldsymbol{u}^n + \Delta\boldsymbol{u}\right)$ where $\boldsymbol{M} \in \mathcal{R}^{dN_n \times dN_n}$ is the mass matrix (diagonal), d is the number of dimensions in the lattice, N_n is the total number of nodes in the lattice, and $\Delta\boldsymbol{x}$ and $\Delta\boldsymbol{u}$ are the incremental change in the position and velocity over the time step. The force at the next time step is then linearized:

$$\boldsymbol{f}\left(\boldsymbol{x}^n + \Delta\boldsymbol{x}, \boldsymbol{u}^n + \Delta\boldsymbol{u}\right) = \boldsymbol{f}^n + \frac{\partial \boldsymbol{f}}{\partial \boldsymbol{x}}\Delta\boldsymbol{x} + \frac{\partial \boldsymbol{f}}{\partial \boldsymbol{u}}\Delta\boldsymbol{u} \tag{20}$$

The derivatives $\frac{\partial \boldsymbol{f}}{\partial \boldsymbol{x}}$ and $\frac{\partial \boldsymbol{f}}{\partial \boldsymbol{u}}$ are evaluated at the current time step n. Because these are derivatives of vectors with respect to vectors, the result is a matrix. These Jacobian matrices are sparse with values only at locations where nodes are connected.

Combining this together yields:

$$\left(\boldsymbol{I} - \Delta t \boldsymbol{M}^{-1}\frac{\partial \boldsymbol{f}}{\partial \boldsymbol{u}} - \Delta t^2 \boldsymbol{M}^{-1}\frac{\partial \boldsymbol{f}}{\partial \boldsymbol{x}}\right)\Delta\boldsymbol{u} = \Delta t \boldsymbol{M}^{-1}\left(\boldsymbol{f}^n + \Delta t \frac{\partial \boldsymbol{f}}{\partial \boldsymbol{x}}\boldsymbol{v}^n\right) \tag{21}$$

where $\boldsymbol{I}$ is the identity matrix [5]. This scheme is theoretically unconditionally stable; however, the linearization process reduces the stability limits on the time step. Given

the increment in velocity, $\Delta \boldsymbol{u}$ from this scheme, the position is updated by $\Delta \boldsymbol{x} = \Delta t \left(\boldsymbol{u}^n + \Delta \boldsymbol{u} \right)$.

The Runge-Kutta family of methods yields higher order of accuracy schemes. The implicit second order scheme is given by:

$$\Delta \boldsymbol{u} = \frac{\Delta t}{2} \boldsymbol{M}^{-1} \left(\boldsymbol{f}^n + \boldsymbol{f}^{n+1} \right) \tag{22}$$

where the same linearization is performed as before. Once the first order Euler method is implemented, upgrading it to the Implicit Runge-Kutta second order scheme is very simple and requires only a few extra multiplications per node.

2.4 Lattice Evolution

The lattice nodes evolve in time due to mass loss caused by chemical reactions and due to the acceleration caused by body and spring/damper forces. The evolution of nodes due to the acceleration is achieved using any time integration appropriate for ordinary differential equations. Explicit Euler integration is used in this work. The change in position of the nodes results in a change in density by holding the mass of the node constant while the new dual-mesh is used to compute the updated volume.

At a given lattice node, a check is performed to determine which, if any, neighbors are exterior nodes marked as a fluid. If a node has a fluid neighbor, the regression distance is computed using an Arrhenius rate law $r = A \exp\left(-E_a/RT\right) \Delta t / \rho_0$ where A is the pre-exponential factor given in $kg/m^2 s$, E_a/R is the activation energy over the gas constant in consistent units, Δt is the discrete time step and ρ_0 is the initial density of the material. The result r is the amount the material regresses in meters.

The node is moved by the distance r along the unit vector away from the fluid node as shown in Figure 9. The resulting dual-mesh is used to update the volume. The node density is held constant throughout the process and the new volume is used to compute the change in mass. When the mass is sufficiently close to zero, the node is converted into an exterior fluid node.

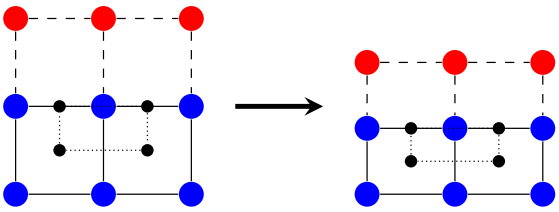

Figure 9: Demonstration of the change in lattice nodes due to chemical reactions when exposed to a fluid

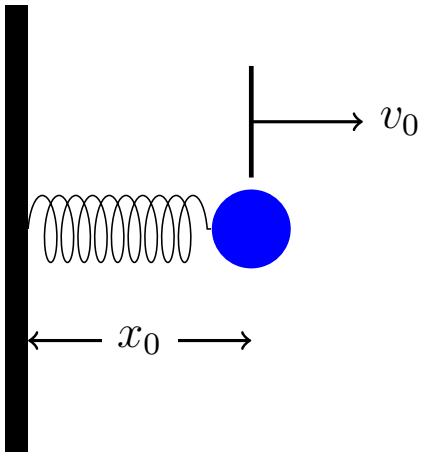

Figure 10: Harmonic oscillator setup for temporal scheme validation

2.5 Formulation Validation

2.5.1 Temporal Accuracy

Validation of the temporal schemes uses a simple harmonic oscillator as shown in Figure 10. The initial displacement is zero and the initial velocity is $0.1\,\mathrm{m\,s^{-1}}$. The spring stiffness is $0.35\,\mathrm{N\,m^{-1}}$ and the mass is $1/18\,\mathrm{kg}$.

The displacement from the initial conditions with time computed with the Implicit Runge-Kutta (RK2) routine is shown in Figure 12. The other numerical schemes generate similar results although the Velocity-Verlet scheme has not yet been validated. The L_2 error in the displacement for the Explicit and Implicit Euler and the Implicit RK2 scheme shown in Figure 11b demonstrates the improved accuracy of the second order scheme.

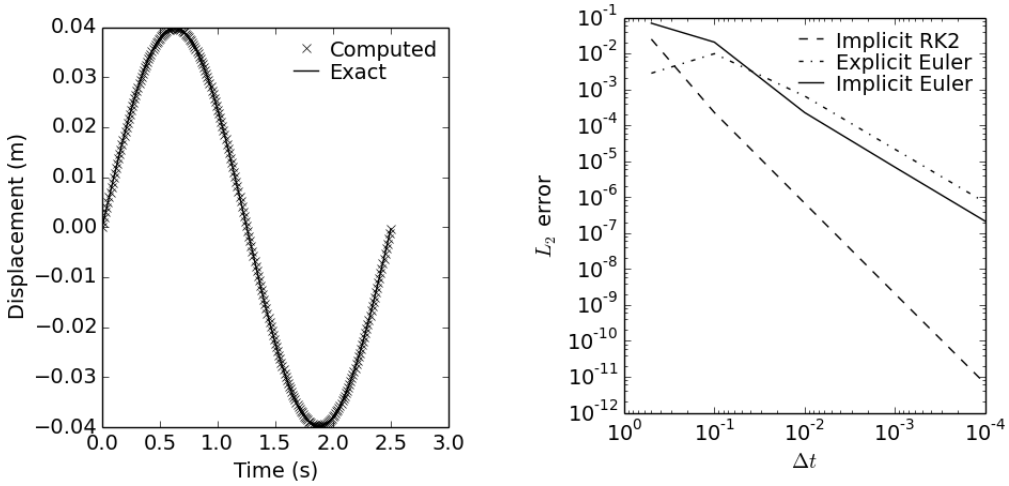

(a) Harmonic oscillator displacement with time

(b) L_2 error in displacement for the harmonic oscillator

Figure 11: Temporal scheme validation using harmonic oscillator

2.5.2 Spatial Convergence

Another canonical test case from structural mechanics is used to verify the spatial convergence of the scheme. A uniform rod undergoing distributed axial tension is discretized with a uniform lattice. The number of points used in the uniform lattice varies to measure the spatial convergence. The left end is fixed and the right end is free. The rod is slender with a Young's modulus of E, cross-sectional area A and total length of L. The load, f, is likewise uniform and distributed axially over the rod.

The governing differential equation is:

$$EAu''(x) = -\frac{f}{L} \tag{23}$$

where $(\cdot)'$ indicates differentiation with respect to x. This may be integrated twice to give:

$$EAu(x) = -\frac{f}{2L}x^2 + Ax + B \tag{24}$$

where A and B are constants determined by the boundary conditions. The left end is fixed implying $u(0) = 0$ and therefore $B = 0$. The right end is free implying $u'(L) = 0$

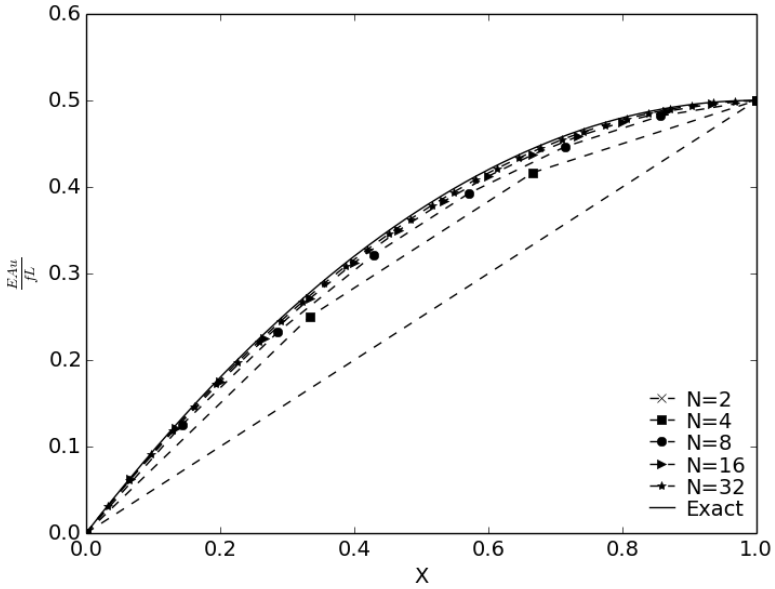

Figure 12: Convergence of MSDM to the exact solution for the axial rod under uniform loading.

resulting in $A = f$. The final solution is therefore:

$$u(x) = \frac{fL}{EA}\left(\frac{x}{L} - \frac{x^2}{2L^2}\right) \tag{25}$$

MSDM is used to compute the solution to this problem for lattices consisting of 2^n nodes where $n \in [1, 5]$. Figure 12 is the resulting displacement of the nodes alongside the exact solution. MSDM converges to the exact solution as the lattice is refined. Notably, the displacement at $x = L$ is always accurate, independent of the number of nodes in the lattice. This case also illustrates that convergence of the integral, peridynamic-based formulation to the differential, classical approach to continuum mechanics cited previously [57].

2.5.3 Wave Propagation

The formation of hotspots in energetic materials due to impact requires the correct prediction of wave propagation through the material. The characteristic speed of a

longitudinal wave through a material (limited to $\nu = 0.25$) is:

$$U = \sqrt{\frac{E}{\rho}} \tag{26}$$

with E the Young's Modulus and ρ the density of the material. Likewise, the characteristic speed of a longitudinal wave through a mass-spring system is:

$$U = \sqrt{k/m} \tag{27}$$

where k is the spring constant and m is the mass of the node. Equating these two expressions and noting that $k = El_0$ and $m = \rho l_0 h_0 d_0$ where l_0 is the length of the representative volume, h_0 is the height and d_0 is the depth yields:

$$\frac{E}{\rho} = \frac{El_0}{\rho l_0 h_0 d_0} \rightarrow 1 = h_0 d_0 \tag{28}$$

Performing the same substitution for longitudinal waves in the direction of the height and the depth of the representative volume gives $l_0 d_0 = 1$ and $l_0 h_0 = 1$. These three equations may only hold if $l_0 = h_0 = d_0$.

This result leads to two important conclusions. First, the grid must be uniform and this is true in both 2 and 3 dimensions. When computing the mass from the density in 2D, the depth of the volume used may not be arbitrary but must be equal to the other lengths. Second, accurate wave speeds are possible regardless of the grid resolution. Coarse or fine grids should generate the correct wave speeds provided the grids are uniform.

A simple test case with a material discontinuity located halfway along the wave propagation direction is used to validate these conclusions. The material properties are chosen such that the characteristic wave speed is identical in both while the characteristic impedance, $Z = \rho U$ is different. The characteristic impedance in the second half of the domain is half that in the first: $Z_1/Z_2 = 2$. An initial velocity disturbance is set at the left edge of the domain and propagates to the right. Both the left and right boundaries are unconstrained. A small amount of damping is added

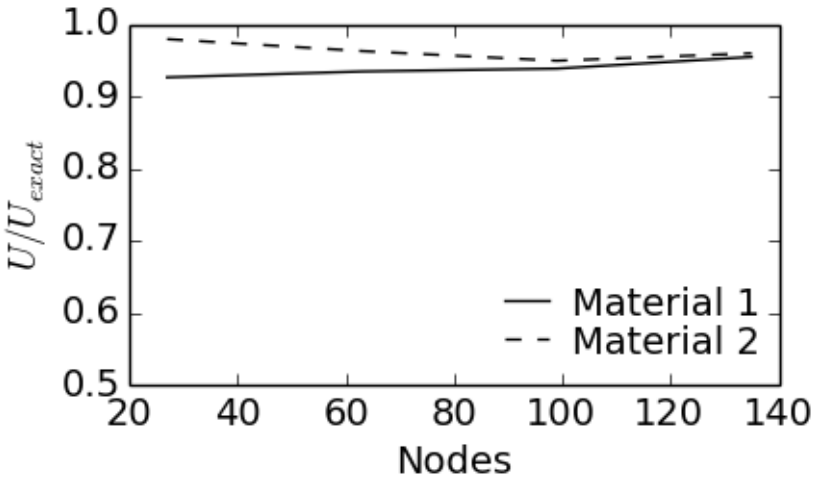

Figure 13: Wave speed error versus grid resolution through a material discontinuity

to eliminate the oscillating on the trailing side of the wave; without this damping, the wave reflected from the material interface is lost in the oscillations. Figure 13 is the ratio of the computed wave speed U to the theoretical wave speed U_{exact} as it varies with grid resolution. The wave speed is slightly under-predicted in both materials with a larger error in the first material at coarser resolutions. This error may be attributed to the damping added to the simulation.

In addition, the material discontinuity and the resulting impedance discontinuity causes the incident wave to generate a transmitted wave into the second material and a left-traveling reflected wave in the first material. This process is shown in Figure 14.

2.6 Surface Regression

Validation of the surface regression uses a uniform material under two different configurations to determine the influence of the structured lattice on the regression. The first test is a square sample of material rotated 30° about the origin with only the surface in the Y-direction exposed as shown in Figure 15a. The other boundary conditions are treated as solid. This creates a surface regression that is not aligned with

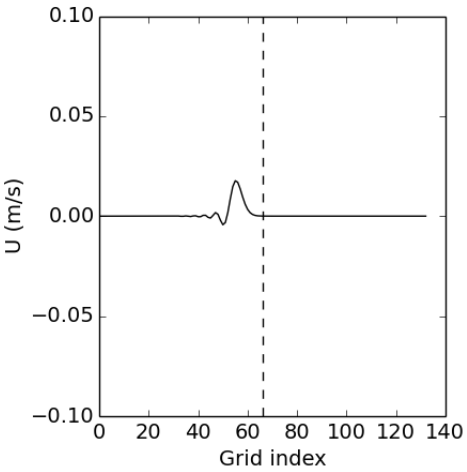

(a) Wave prior to material interface

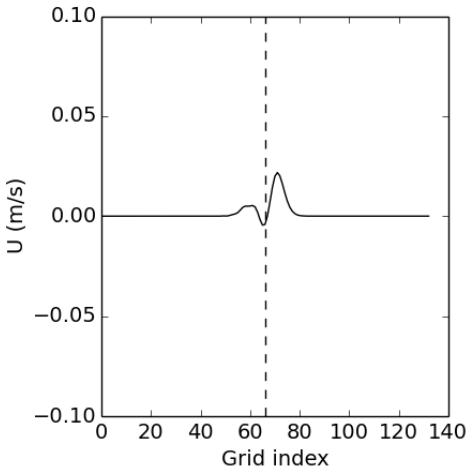

(b) Wave at material interface

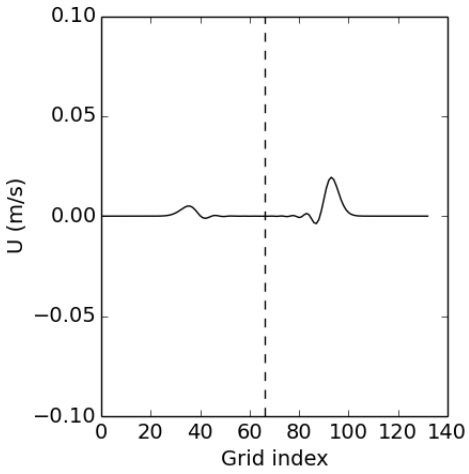

(c) Transmitted and reflected waves

Figure 14: Wave transmission through a material discontinuity

the computational coordinates. The surface regresses in the Y-direction and remains planar throughout as indicated in Figure 15b. The second configuration is a circular material sample exposed on all sides to test a more complex regression. The material is expected to remain circular while decreasing in size throughout the regression. The initial and final states are shown in Figure 16. Both tests indicate that the surface regression may occur along arbitrary directions relative to the computational coordinates.

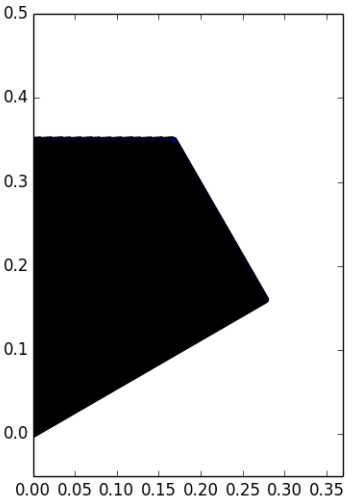

(a) Initial configuration for the rotated material sample.

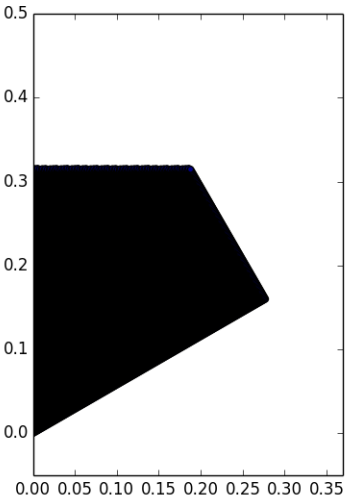

(b) Surface at later time indicating planar regression is maintained

Figure 15: Planar regression in a rotated material sample

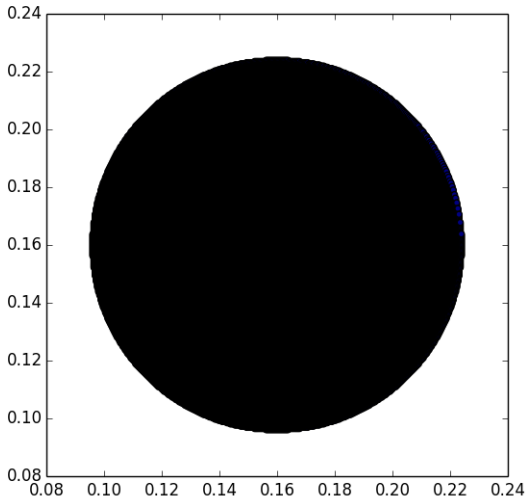

(a) Initial configuration for the circular material sample.

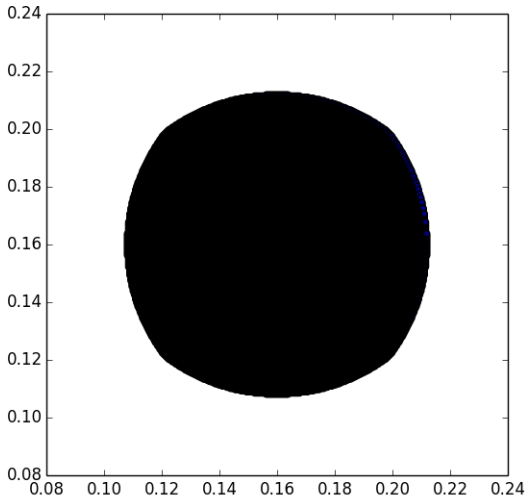

(b) Final state of the circular material sample

Figure 16: Surface regression in a circular material sample

CHAPTER III

HETEROGENEOUS SOLID PROPELLANT PYROLYSIS

The random packing of Ammonium Perchlorate (AP) in Hydroxl-Terminated Polybutadiene (HTPB) binder is a canonical solid propellant used to establish computational models. One dimensional models based on the BDP flame structure [11] are capable of accurately predicting the burn rates of AP-HTPB propellants [11, 16, 21] but lack the ability to predict detailed surface features of the propellant. These detailed structures have an important influence on the global stability of the propellant in rocket applications [4]. The ability of MSDM to capture both the global trends and the micro-scale surface structures is therefore essential.

3.1 Computational Setup

A 2D slice of randomly packed AP particles embedded in HTPB binder measuring 0.24 cm by 0.24 cm is discretized by 10000 nodes. The AP particles measure 200 microns in diameter and make up 80% of the weight of the propellant [21]. The packing is generated using the RocPack code [35] and shown in Figure 17a. The surface temperature of the propellant is assumed to be constant and related to the flame stand-off distance [11]. The Arrhenius rate parameters for AP are $A_{AP} = 5.0e6$ kg/m^2/s and $E_{a,AP} = 92109.6$ J/mol [11]; for HTPB, $A_{HTPB} = 3.0e4$ kg/m^2/s and $E_{a,HTPB} = 62800$ J/mol [21]. The momentum equation is not solved during this process as there are no mechanical effects.

3.2 Results and Discussion

The burn rate is computed by taking the difference of the average height of the remaining propellant at two instants in time. The computed burn rates are in Table

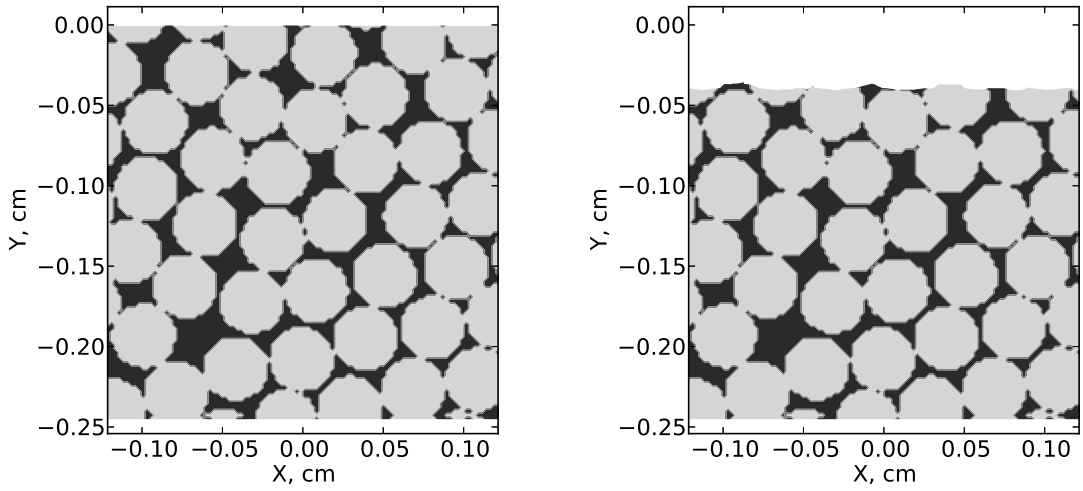

(a) Initial distribution of AP in HTPB (b) Surface of propellant at 0.1 s

Figure 17: Burning AP-HTPB composite propellant; AP particles are gray while HTPB is black

Table 1: Burn rates (cm/s) of AP-HTPB with and without TiO_2 nanoparticle impregnation

Temperature (K)	Pressure (MPa)	Burn rate, no TiO_2	Burn rate, TiO_2
823	1.12	0.3978	0.5411
860	5.44	0.6953	0.9510
908	15.38	1.3388	1.8364

1. The surface of the propellant when $T = 823$ K at 0.1 s is in Figure 17b and has a non-uniform structure contour due to the different burning rates of the AP and HTPB.

The surface regression rate increases with pressure and is experimentally and numerically shown to increase linearly with the logarithm of pressure [21]. Catalytic additives are mixed into the AP-HTPB propellants to accelerate the regression rate which is modeled by increasing the Arrhenius pre-exponential factor, A, by a new factor Ω. For these simulations, $\Omega = 1.41$ corresponding to a 1% TiO_2 spray-dried impregnation [21]. MSDM predicts the variation in burn rate with pressure well within the experimental errors in the work of Frazier *et al* both with and without

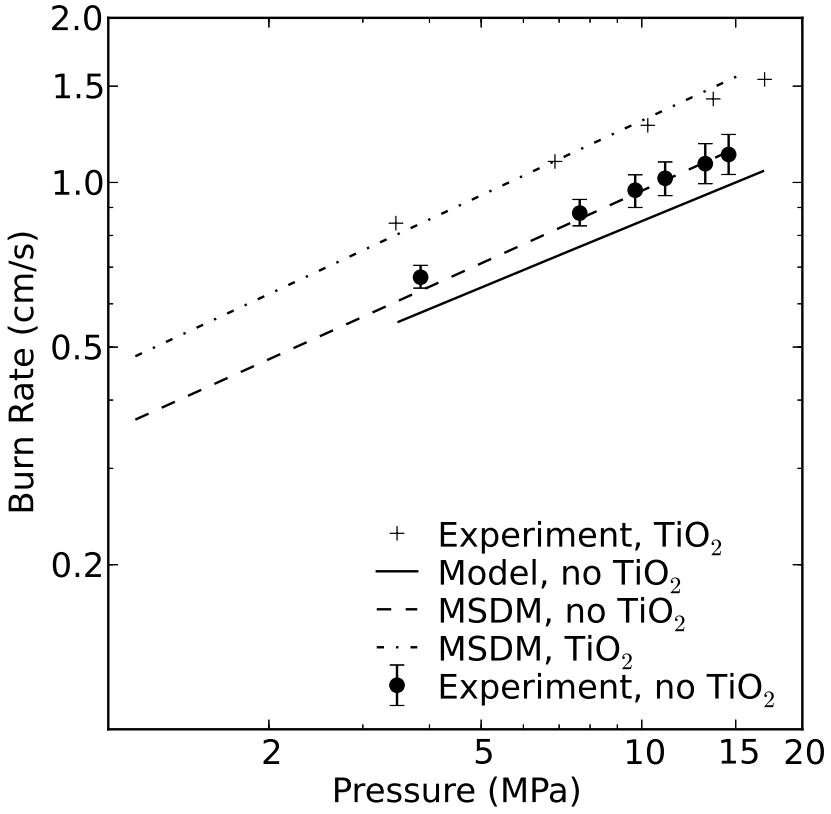

Figure 18: Surface burn rate of AP-HTPB randomly packed propellant with and without the nanoparticle catalytic additive TiO_2. Experiment and model data from Frazier et al [21]

TiO_2 impregnation [21]. Figure 18 compares the current results to the experiments and existing model. The surface of the propellant at 0.05 s for the various cases in Table 1 is shown in Figure 19. There is considerable variation in the surface contours for a fixed temperature with and without the nanoparticle catalytic additive; MSDM captures the micro-scale variation in the surface.

The surface temperatures simulated range from the upper end of regime I to the end of regime II shown in Figure 4. Boggs described the characteristics of the surface regression for a single crystal of AP across these regimes [12]. In regime I, corresponding to the 823 K case, the regression is steady and planar. Inspection of the AP crystals in Figure 19a reveals the surface of the AP crystals is approximately planar

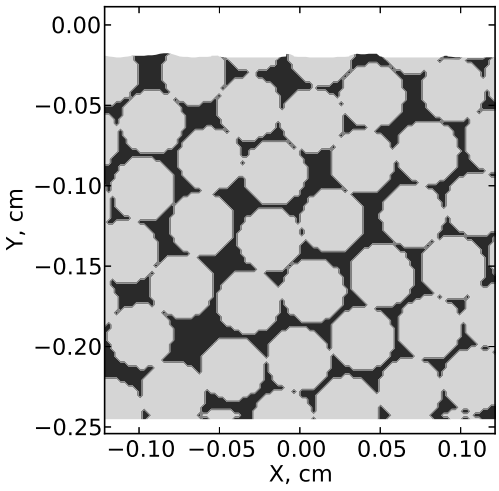

(a) No nanoparticles, 823 K

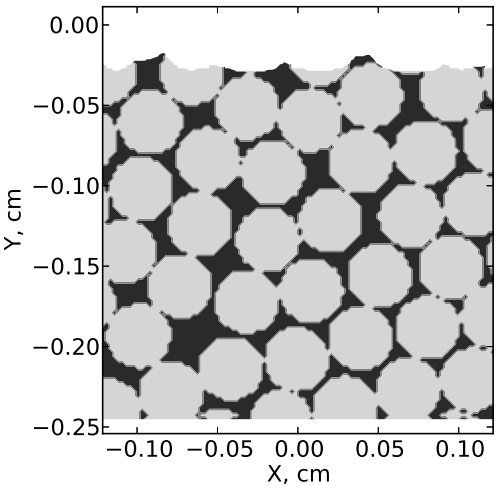

(b) Nanoparticles, 823 K

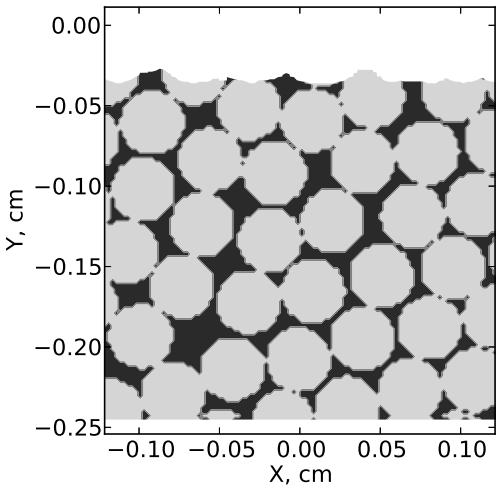

(c) No nanoparticles, 860 K

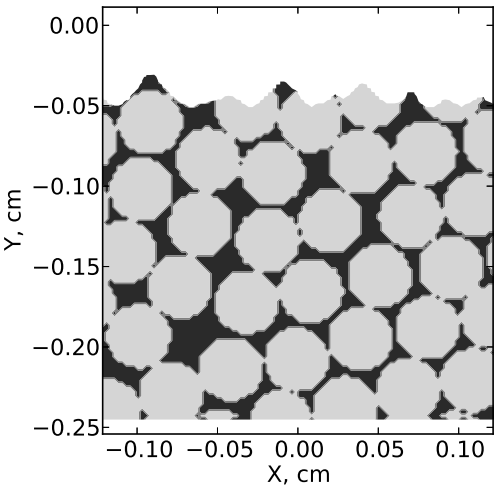

(d) Nanoparticles, 860 K

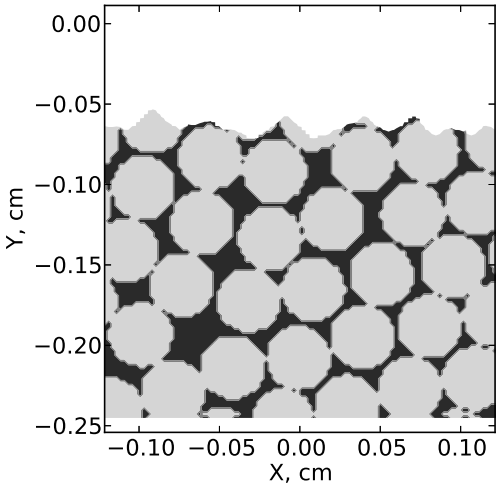

(e) No nanoparticles, 908 K

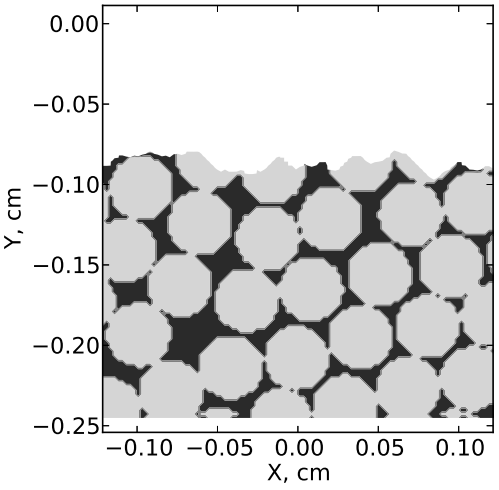

(f) Nanoparticles, 908 K

Figure 19: Propellant surface at 0.05 s

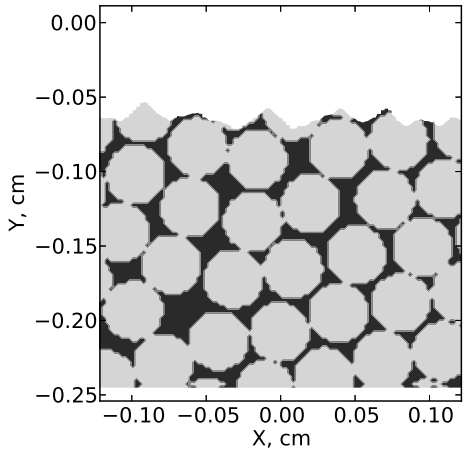

(a) Simulation at 908 K

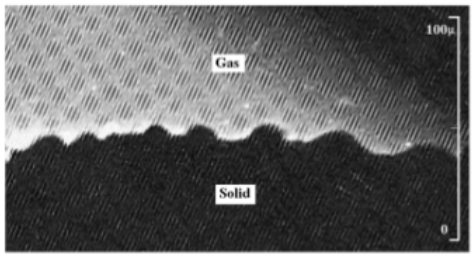

(b) Photo of AP-HTPB surface after burning (from [33])

Figure 20: Comparison of simulation to experimental image of AP-HTPB surface after burning

as expected. In regime II, Boggs describes the regression of AP crystals as steady and macroscopically planar, but close inspection of the crystals reveals a number of ridges and valleys. These ridges and valleys become sharper and more needle-like during the transition to regime III. At 860 K, the surface of the AP crystals reveals micro-scale ridges and valleys as described experimentally. At 908 K, which occurs close to the transition to regime III, the ridges and valleys are more pronounced and sharper. These qualitative descriptions match those from experiments into the combustion of AP crystals [12]. Figure 20 provides an additional qualitative comparison to an experiment of AP-HTPB propellant combustion [33].

For these simulations, the surface temperature is held constant and is not part of the solution procedure. The surface temperature is determined by the flame stand-off distance, which decreases as the ambient pressure increases [11]. Prediction of the surface temperature is therefore a problem requiring both fluid and solid phases. This coupling is outside of the scope of this work and therefore absent from these simulations. When provided surface temperatures, whether imposed and held constant as done here or when determined through a fluid-solid coupled simulation, MSDM is

capable of predicting the fine-scale structures and global trends in solid propellant combustion.

CHAPTER IV

HOTSPOT FORMATION IN HETEROGENEOUS EXPLOSIVES

Polymer bound explosives (PBXs) fulfill a wide range of military and industrial applications. They are composed of an energetic crystal powder suspended in a polymer matrix. The resulting mixture may be cast or molded into a variety of shapes or casings depending on the intended application. The polymer binder serves two primary functions: first, it enables shaping or casting of the energetic material; second, it absorbs the mechanical energy imparted by handling or impacting the material, reducing the likelihood of an accidental detonation of the PBX.

Mechanical impacts generate a pressure wave within the PBX which may or may not trigger a detonation. Localized heating within the material, known as hot spots, as the pressure wave moves through discontinuities located within are the commonly accepted mechanism for transitions to detonation [50]. These discontinuities may be defects such as voids or cracks, or they may be due to material inhomogeneities such as material interfaces.

The exact mechanisms of hot spot formation remain elusive [1]. Simulations of void collapse yield insight into the heating due to adiabatic compression and viscoplastic work as a mechanism for hot-spot formation [58, 59]. Finite-element simulations of realistic PBXs undergoing low-speed impacts reveal localized heating along the material interfaces [6–8]. Molecular dynamics simulations of an idealized, non-planar material interface under high-speed impacts also indicate that heating at the material interface due to impedance differences in the materials [1, 2].

An *et al.* [2] studied a highly shocked, sawtooth interface between 1,3,5-trinitroperhydro-1,3,5-triazine (RDX) and hydroxyl-terminated polybutadiene (HTPB) binder. Later work [1] also studied 2,2-Bis(nitroxymethly)-1,3-propanedio dinitrate (PETN) and silapentaerythritol tetranitrate (Si-PETN) in the same configuration with HTPB. In all cases, significant heating occurred at the tip of the sawtooth interface. This heating occurred in three phases [1]:

1. Initial heating due to adiabatic compression of the material as the shock arrives;
2. Slight cooling as the shock passes into the softer binder material generating expansion waves in the energetic material due to impedance differences;
3. Post-shock heating due to chemical reactions (negligible in the RDX and PETN but significant in the Si-PETN).

Low-speed impact simulations indicate similar processes. The initial heating is due primarily to the elastic compression of the material while at late times the heating mechanisms change to plastic work and viscous dissipation within the material [8].

The aforementioned studies focus on the mechanisms by which hotspots form at material interfaces while the influence of material properties on the hotspot structure and locations is not studied in detail. An *et al* did a cursory study by varying the binder density in an attempt to eliminate the hotspot in the highly shocked, sawtooth RDX-HTPB simulation [2]. Their study indicates that a reduction in the binder density eliminates the hotspot.

In this work, the influence of the material properties on the hotspot structure is determined. Similar studies to An *et al* using variations in the binder density are performed. The influence of the energetic crystal properties on hotspot structure is also determined by using the common explosives RDX, octahydro-1,3,5,7-tetranitro-1,3,5,7-tetrazocine (HMX), PETN and the novel explosive dihydroxylammonium 5,5'-bistetrazole-1,1'-diolate (TKX-50). Finally, the hotspot structure's dependence on the

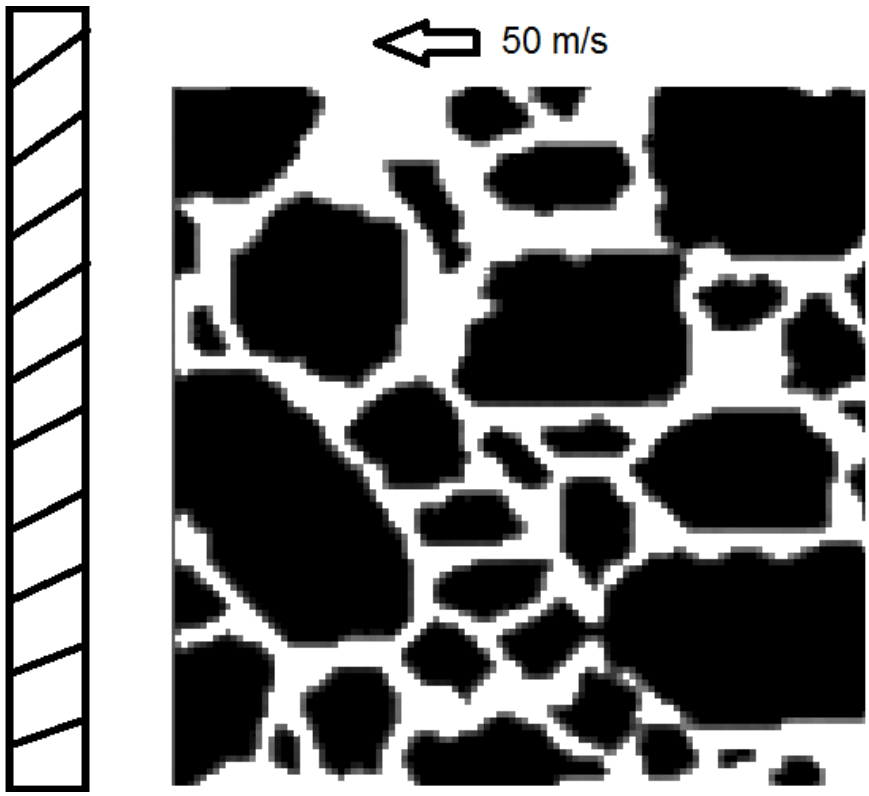

Figure 21: Digitized photo of PBX used to simulate hotspot formation due to impacts. Black represents the energetic crystals while white is binder.

impact velocity is studied. Statistical models of the hotspot structure for HMX and RDX as a function of impact velocity are generated.

4.1 Computational Setup

A randomly packed material is created from a digitized image [8] and is shot at a wall with velocities between $50\,\mathrm{m\,s^{-1}}$ and $250\,\mathrm{m\,s^{-1}}$ as shown in Figure 21. The grid uses a single node per pixel in the image resulting in a lattice discretized by 432x432 nodes. The left boundary condition is a rigid wall allowing slip in the transverse directions. The remaining boundaries are free. The initial temperature is uniform at $300\,\mathrm{K}$.

To test the results of An *et al* [2], the binder properties are varied to create artificial binders with densities matching that of the energetic crystal and half that of the original binder (Estane) in addition to a density altered to create a binder with

Table 2: Material properties for all energetic crystals.

	HMX	RDX	PETN	TKX-50
Γ (-)	0.7 [63]	0.93 [27]	1.15 [36]	0.6894
ρ (kg/m^3)	1580.0 [8]	1799.0 [27]	1770.0 [36]	1877.0 [24]
c_v (J/kgK)	1757.28 [63]	1456.0 [27]	1009.0 [36]	1236.44 [24]
E (MPa)	25325.0 [54]	20200.0 [53]	11800.0 [62]	52194.0 [24]
K_T (GPa)	11.3 [54]	12.0 [53]	11.0 [46]	32.719 [24]

Table 3: Material properties for all binder variants.

	Estane	Half-Density	Density-Matched	Impedance-Matched
Γ (-)	1.0 [28]	1.0	1.0	1.0
ρ (kg/m^3)	1280.0 [28]	640.0	1580.0	6402.16
c_v (J/kgK)	1481.14 [28]	1481.14	1481.14	1481.14
E (MPa)	6250.0 [28]	6250.0	6250.0	6250.0
K_T (GPa)	4.3 [28]	2.15	5.31	21.51

matching impedance. These studies are performed at $50\,\mathrm{m\,s^{-1}}$ with HMX energetic crystals.

Additional studies for a single binder, Estane, vary the energetic crystal to determine the influence on hotspot formation and location. Table 2 provides the material properties used for each of the crystals and and Table 3 provides the binder variants.

4.2 Binder Variants

An *et al* proposed reducing the binder density by a factor of two to eliminate hotspots in a highly-shocked sawtooth PBX [2]. MSDM simulations using HMX and Estane with altered densities also reach the same conclusion. Figure 22 compares the temperature of a representative hotspot for all four binder variants. Only the low density binder eliminates the hotspot, bringing the peak temperature down by 17 K or 5%. The other variants generate hotspots with temperatures comparable to the original Estane binder. The temperature fields for all variants are shown in Figure 23. The half-density binder in Figure 23b shows no hotspots while the impedance-matched binder in Figure 23c shows much larger regions of elevated temperature.

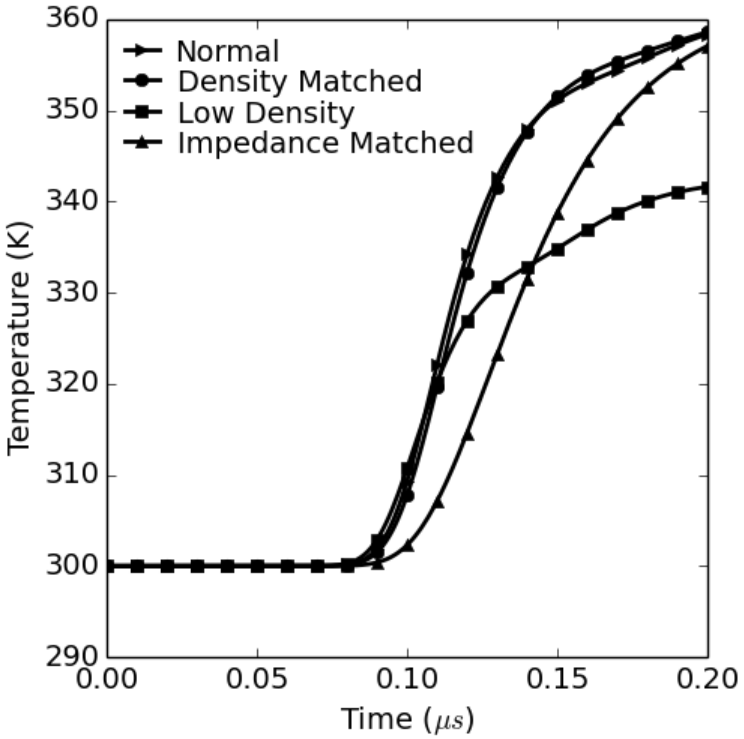

Figure 22: Comparison of a representative hotspot's temperature with time for all binder variants tested.

Figure 23 shows additional differences in the hotspot structure for the binder variants. The temperature contour for the impedance-matched binder (Figure 23c) shows much larger regions of elevated temperature than the normal Estane or the density-matched Estane.

4.3 Hotspot Detection

The identification of hotspots is inherently subjective [23]. The subjectivity enters through the selection of the threshold temperature, above which a region is considered a hotspot. Hotspots are, by definition, an anomalous region of elevated temperature. The method used to determine the hotspot threshold temperature is the same as that used by Gilbert *et al* [23]. The temperature along a line through what appears to be a hotspot and along a line through a region with no hotspot is plotted as demonstrated in Figure 24. The threshold temperature is chosen to isolate only the anomalous regions and is different for each impact velocity. Increasing the threshold temperature will do little to change the resulting hotspot field as the anomalous regions are at a significantly elevated temperature relative to the regions without hotspots. However, reducing the threshold temperature will result in false-positives by identifying normal regions as hotspots. The threshold temperature is taken to be the minimum temperature that eliminates these false positives by taking the temperature tangent to the normal regions as shown in Figure 24. Due to the similarity in results to be discussed later in the chapter, the threshold temperatures for HMX and RDX are the same.

Once the threshold is selected, hotspots may be identified. For each case, the 2D set of results in time are stacked together to make a 3D dataset in (x, y, t) space. Iso-surfaces using the threshold temperature are then extracted, providing information such as peak temperature within the volume and the area of the hotspot. Statistical models for HMX and RDX use this structural information as described later in the

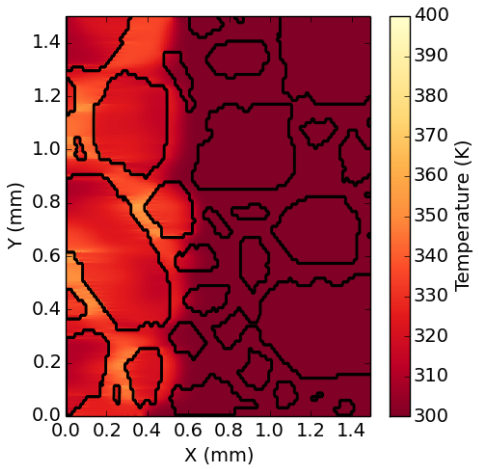

(a) Temperature distribution with normal Estane binder.

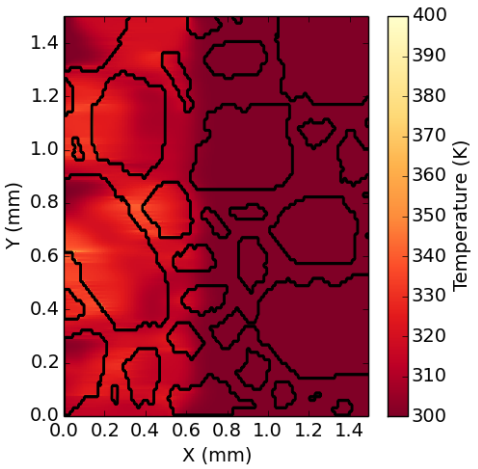

(b) Temperature distribution with half-density binder.

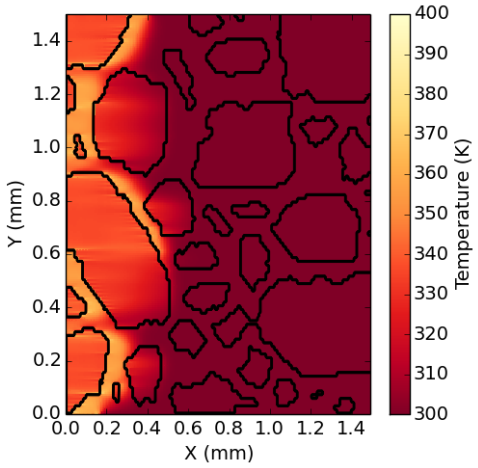

(c) Temperature distribution with impedance-matched binder.

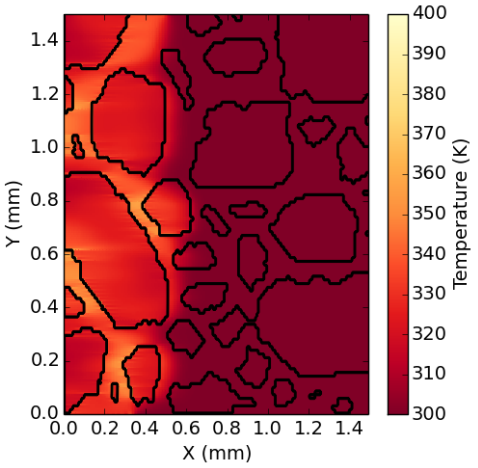

(d) Temperature distribution with density-matched binder.

Figure 23: Influence of binder density on hotspot temperature.

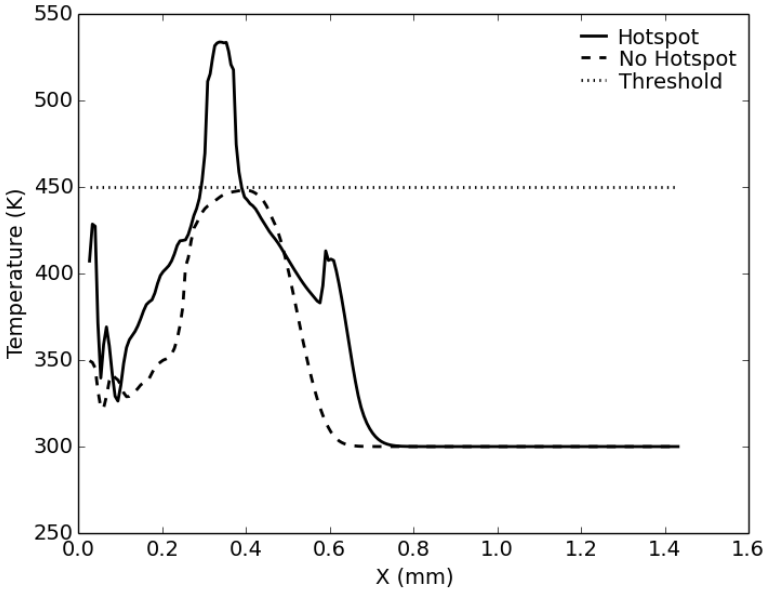

Figure 24: Illustration of temperature threshold selection for hotspot detection procedure.

chapter.

4.4 Energetic Crystals

The method described in the previous section is performed for the simulations of each impact velocity and energetic crystal. Previous studies indicate that the peak temperature of the hotspot is a more significant factor in the transition to detonation than the mean temperature [23]. Figure 25 is the peak temperature of all the confirmed hotspots for each material and impact velocity.

Due to the random nature of the energetic crystal packings in binder, measurements of hotspot characteristics must be statistical in nature. There are three primary trends in the hotspot intensity. First, within the traditional energetic materials HMX, RDX and PETN, the hotspot intensity is relatively independent of material and the peak temperature is linear with respect to the impact velocity. Second, for all materials the variation for a given impact velocity in peak temperature increases as the

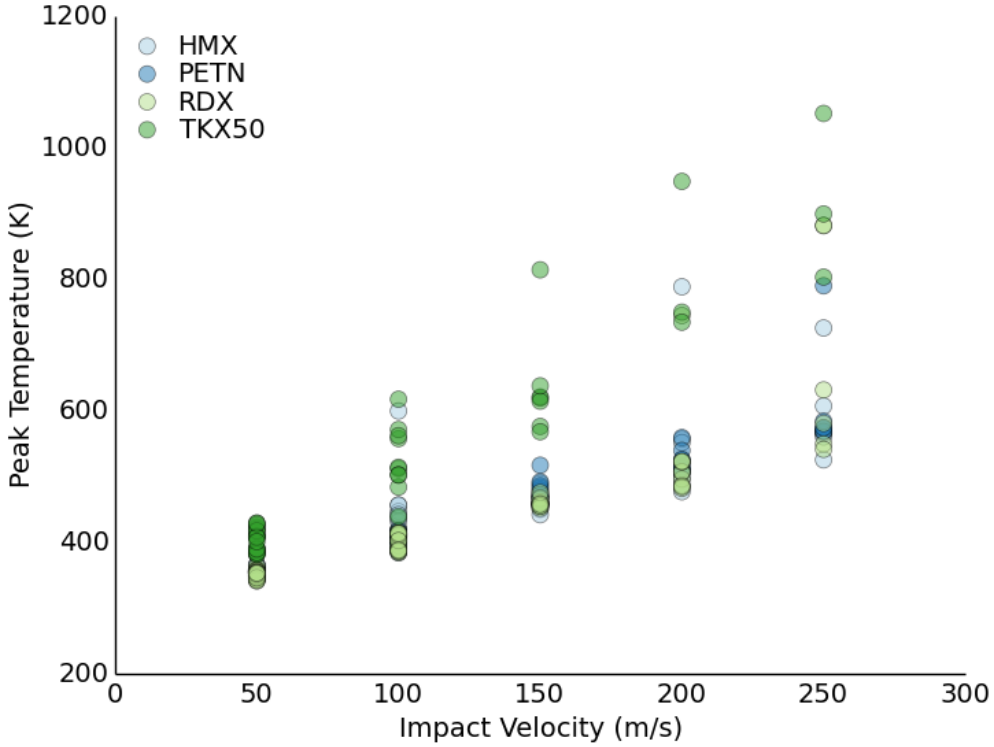

Figure 25: Confirmed hotspot peak temperature for each impact velocity and energetic crystal

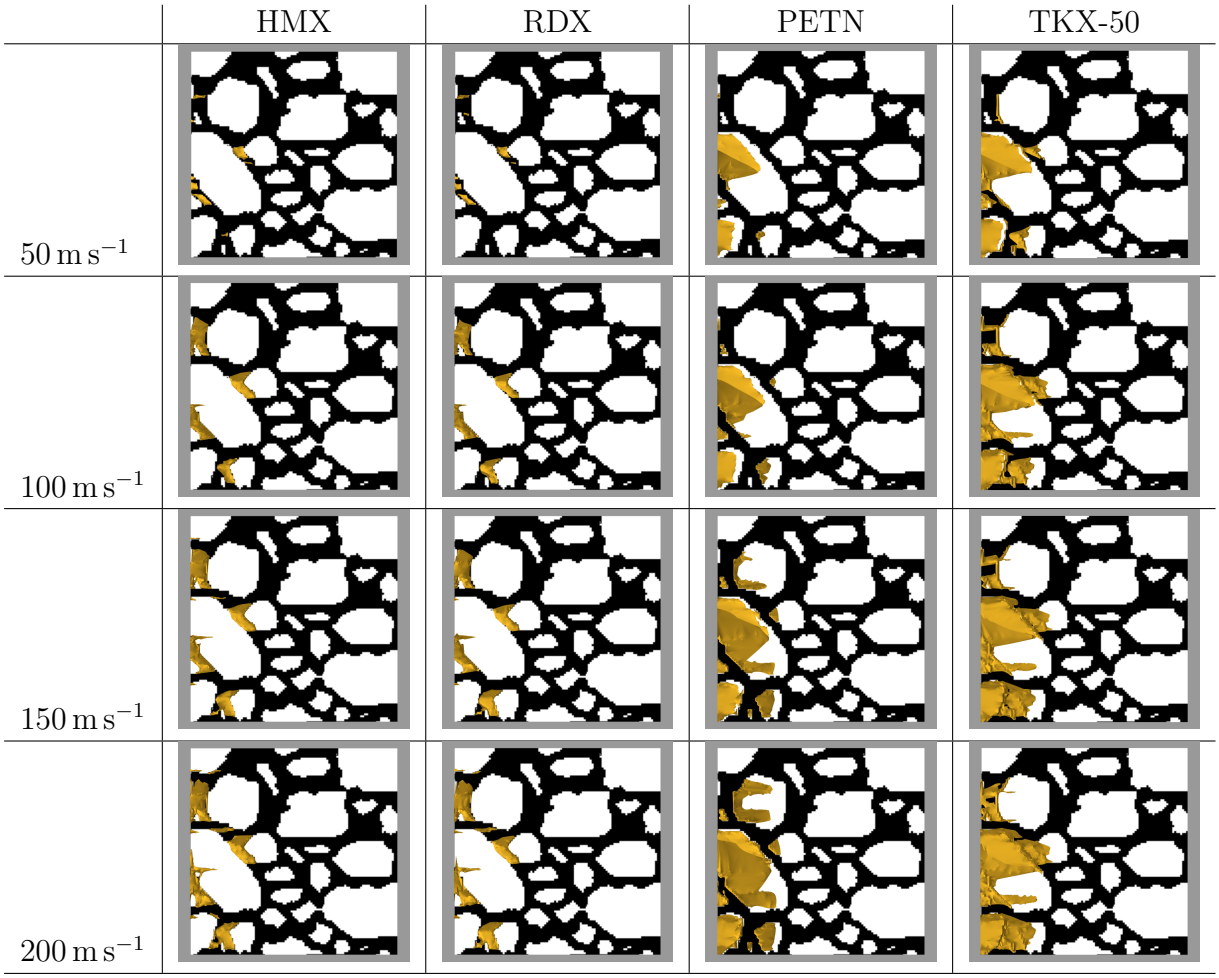

Figure 26: Isosurfaces (gold color) of confirmed hotspots viewed along the time axis for each impact velocity and energetic crystal (crystals are white, binder is black). Note: the isosurface threshold temperature varies as specified previously.

impact velocity increases. The linearity and variation are consistent with other simulations [23]. Finally, the peak temperature for TKX-50 is also linear with impact velocity; however, the peak temperature for several confirmed hotspots is consistently higher than the other materials for each impact velocity.

The location of each hotspot is crucial to understanding the differences between the materials and why the temperature of some hotspots in TKX-50 is higher than the other materials. Figure 26 shows the locations of confirmed hotspots in the explosive for each impact velocity and material. The HMX and RDX results are very similar

and the hotspots are located primarily in the binder between crystals where the distance between two crystals is small. Several hotspots are in the same location for all impact velocities. For these hotspots, the peak temperature and the hotspot size increase as the impact velocity increases. Additional hotspots are formed at higher impact velocities where the gap between crystals is larger. The similarity in hotspot location, shape, and peak temperatures allows the combination of both datasets to generate statistical models.

The PETN hotspots are fundamentally different than those in the RDX and HMX packings. The hotspots in PETN are located primarily within the energetic crystal and not in the binder material for all impact velocities. The Young's modulus for PETN is approximate half that of RDX and HMX leading to more compression within the PETN crystals. This higher compression causes more heating within the crystal itself and less energy transmitted into the binder (resulting in lower heating). Although the crystals are composed of a single, uniform material, their shape is irregular, resulting in non-uniform compression within the crystal. This non-uniformity generates hotspots with unique shapes in each of the crystals.

TKX-50 exhibits additional differences. The hotspots in these simulations are located both within the crystal and the binder material. The higher temperature hotspots are located within the crystal while the hotspots with similar temperature to the HMX and RDX hotspots occur within the binder. Again, the material properties justify these observations. The Young's modulus for TKX-50 is significantly larger than the other materials, more than twice as large as that of HMX. This efficiently transmits the compression wave through the crystal into the binder causing the hotspots to form between crystals. However, the isothermal bulk modulus is approximately 2.5 times larger than that of HMX (while Γ and c_v are comparable to HMX and RDX respectively). Although there is less compression in the TKX-50 crystals

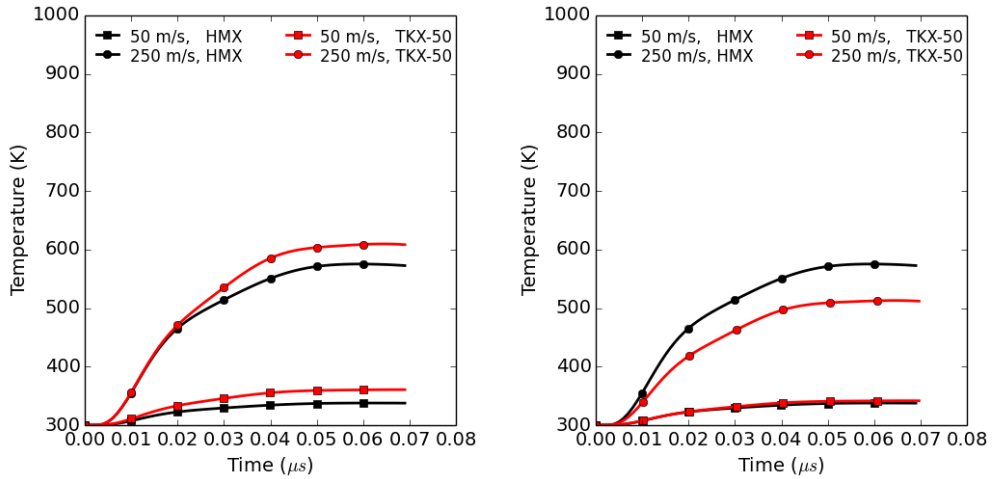

(a) Representative hotspot temperature with larger value of Young's modulus for TKX-50

(b) Representative hotspot temperature with correct value of Young's modulus for TKX-50

Figure 27: Influence of energetic crystal elastic properties on hotspot temperature.

relative to the HMX and RDX crystals, the increase in temperature with compression is larger. Therefore, like HMX and RDX, the Young's modulus results in lower compression and more efficient wave transmission into the binder creating hotspots between crystals. Like PETN, hotspots form within the crystal as well although as a result of different material properties.

Additional insight into the hotspot structure as a function of energetic crystal elastic properties is provided by early simulations of TKX-50 using preliminary and unconverged results from QMD simulations. Figure 27 shows the temperature of a hotspot in the binder located between two crystals. This hotspot is in the same location for both the HMX and the TKX-50 simulations and is representative of the other hotspots located in the binder portion of the material. Figure 27a are the results for TKX-50 using a Young's modulus of 54 239 MPa, a value 4% larger than the correct value of 52 194 MPa used in the updated simulation in Figure 27b. The hotspot formed using the larger value for the Young's modulus is 16% hotter at it's peak than the hotspot formed using the converged value.

4.5 Statistical Models of Hotspot Intensity

Gilbert *et al* simulated the compaction of granular HMX by pistons between $300\,\mathrm{m\,s^{-1}}$ and $500\,\mathrm{m\,s^{-1}}$ [23]. The authors use a hotspot detection method similar to the one previously described to extract structural information about the hotspots. This information is then used to construct probability density functions (PDFs) for each impact velocity.

The same procedure is performed using the data from the HMX and RDX simulations. The hotspots in those datasets are indistinguishable so a single model is generated for both materials. For each impact velocity, the peak temperatures of all of the hotspots are extracted. Trial PDFs are then fit to each dataset using maximum likelihood estimation (MLE) and the goodness-of-fit is measured for each dataset. The PDF that maximizes the goodness-of-fit for all of the datasets is chosen as the best fit for the data and the parameters generated by the MLE are retained. In order to determine and assess the relationships between impact velocity and the PDF parameters, only 3 of the 5 impact velocities are fit and the remaining 2 datasets are then used to evaluate the relationships. The $150\,\mathrm{m\,s^{-1}}$ and $250\,\mathrm{m\,s^{-1}}$ datasets are the two used for evaluation. Confidence intervals for the PDF parameters are computed to determine the uncertainty in the values.

To prevent any user-bias in the trial PDFs, the MLE procedure is performed for every continuous statistical distribution in the SciPy statistics package (version 0.14.0) [32]. The PDF that maximizes the goodness-of-fit for the three datasets is the Gumbel distribution given by Equation 29. This is a two-parameter specialization of the Generalized Extreme Value Distribution and is used to model extremes in datasets [26]. The two parameters are the mean, μ, and the shape, β.

$$f(x) = \frac{1}{\beta} e^{\left(-\frac{x-\mu}{\beta} + e^{-\frac{x-\mu}{\beta}}\right)} \tag{29}$$

Figure 28 shows the histograms of the hotspot peak temperatures for the $50\,\mathrm{m\,s^{-1}}$,

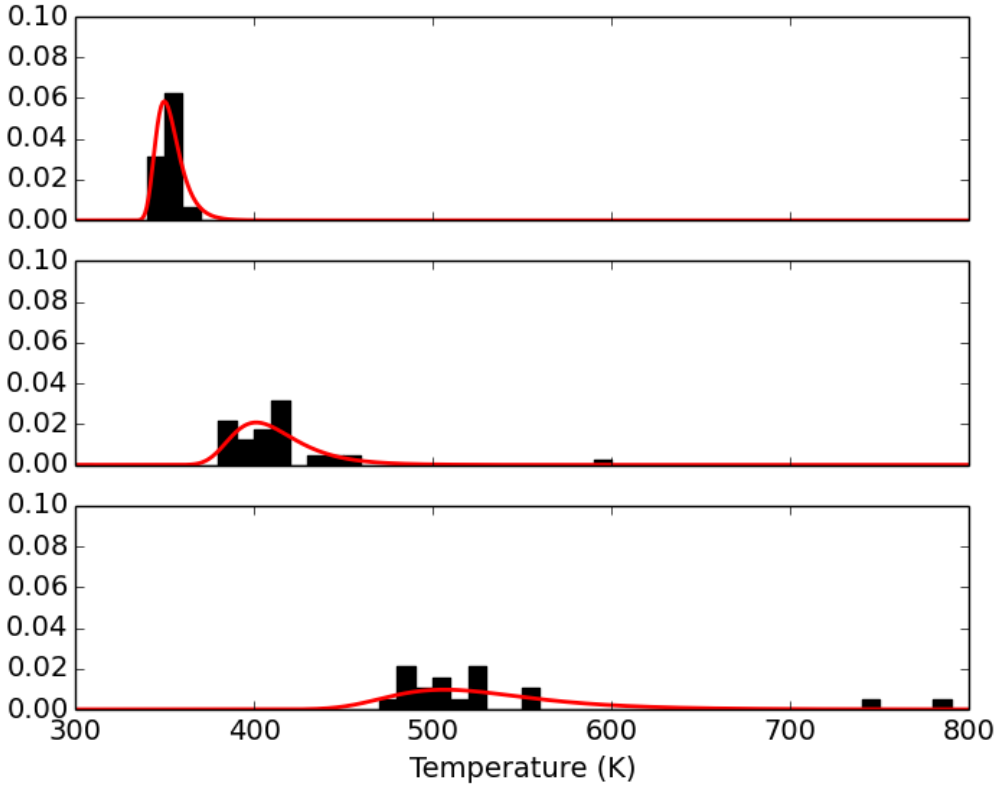

Figure 28: Hotspot peak temperature histograms with the resulting best-fit PDFs for the $50\,\mathrm{m\,s^{-1}}$, $100\,\mathrm{m\,s^{-1}}$ and $200\,\mathrm{m\,s^{-1}}$ simulations (from top to bottom)

$100\,\mathrm{m\,s^{-1}}$ and $200\,\mathrm{m\,s^{-1}}$ simulations (from top to bottom). The resulting values for μ and β are given in Table 4. Both parameters are linear with impact velocity as shown in Figure 29.

The parameters for the $150\,\mathrm{m\,s^{-1}}$ and $250\,\mathrm{m\,s^{-1}}$ are computed from the linear regressions and the resulting distribution is shown in Figure 30. The goodness-of-fit is measured by the Kolmogorov-Smirnov test [41]. There are 18 samples in the $150\,\mathrm{m\,s^{-1}}$ dataset and 15 samples in the $250\,\mathrm{m\,s^{-1}}$ dataset. The null hypothesis is that the samples in each dataset are described by the Gumbel distribution with mean and shape parameters defined by the linear regression from the MLE parameters based on the other datasets. The alternative hypothesis is that the datasets are drawn from a different distribution. The test is two-sided and the significance level required to

Table 4: Mean and shape parameters for the Gumbel distribution generated by maximum likelihood estimation.

	μ	β
$50\,\mathrm{m\,s^{-1}}$	349.90	6.29
$100\,\mathrm{m\,s^{-1}}$	401.30	17.67
$200\,\mathrm{m\,s^{-1}}$	506.61	37.97

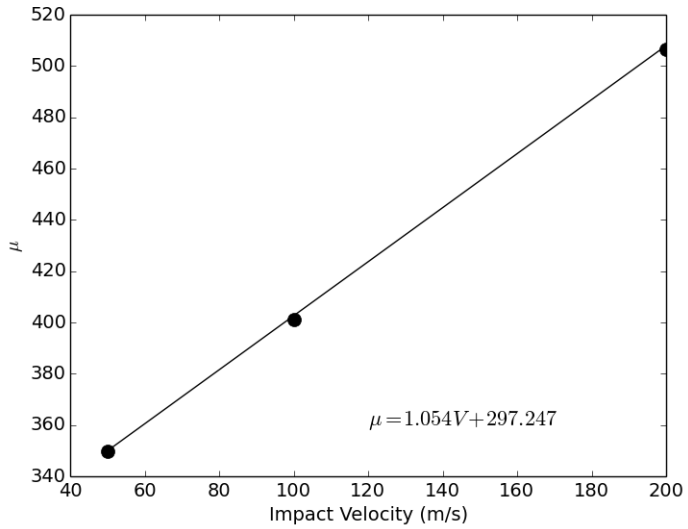

(a) Linear regression of the MLE-determined mean parameter

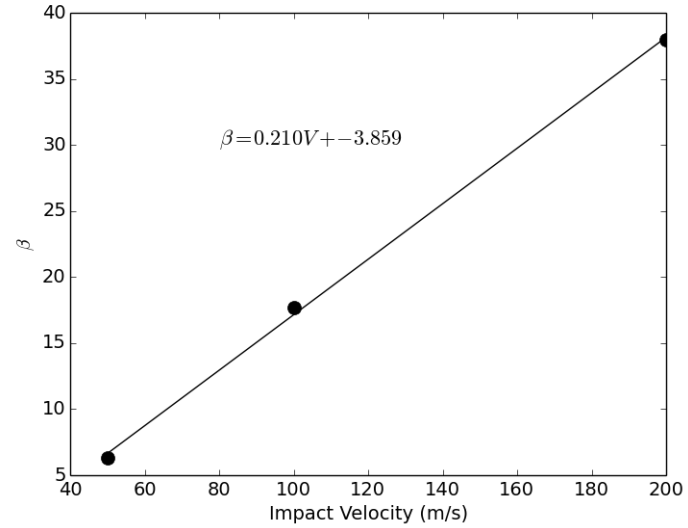

(b) Linear regression of the MLE-determined shape parameter

Figure 29: Mean and shape parameters as a function of impact velocity.

Table 5: Confidence intervals for the MLE-determined mean and shape parameters.

	95% CI μ	95% CI β
$50\,\mathrm{m\,s^{-1}}$	$350.02 - 350.05$	$5.93 - 5.96$
$100\,\mathrm{m\,s^{-1}}$	$401.44 - 401.55$	$17.46 - 17.51$
$200\,\mathrm{m\,s^{-1}}$	$507.41 - 507.75$	$37.46 - 38.04$

reject the null hypothesis, α, is taken to be 0.05.

The resulting P values from the test are 0.0914 and 0.4375 respectively. The null hypothesis may be rejected if $P < \alpha$. In other words, hotspot temperatures for the $150\,\mathrm{m\,s^{-1}}$ and $250\,\mathrm{m\,s^{-1}}$ cases may be described by the distributions generated by the linear regressions for the mean and shape parameter.

Quantifying the uncertainty in the MLE parameters is the final task. One may ask the following question: given a statistically similar random packing, what range will contain the mean value of μ and β for the Gumbel distribution in 95% of the simulations? This range provides an estimate of the uncertainty in the expected value of these parameters that may be expected by running additional simulations of statistically similar packings. The confidence intervals are computed by generating 10000 new datasets from the original datasets for each impact velocity to ensure convergence of the values. These new datasets are generated using boostrap resampling with replacement [19].

Table 5 gives the confidence intervals for the mean and shape parameter. For the mean parameter, the largest confidence interval is 0.3 K, indicating very little variation from these results is expected for other, statistically similar random packings. For the shape parameter, the largest confidence interval spreads approximately 0.6 K, representing a variation of approximately 1.5% in this parameter.

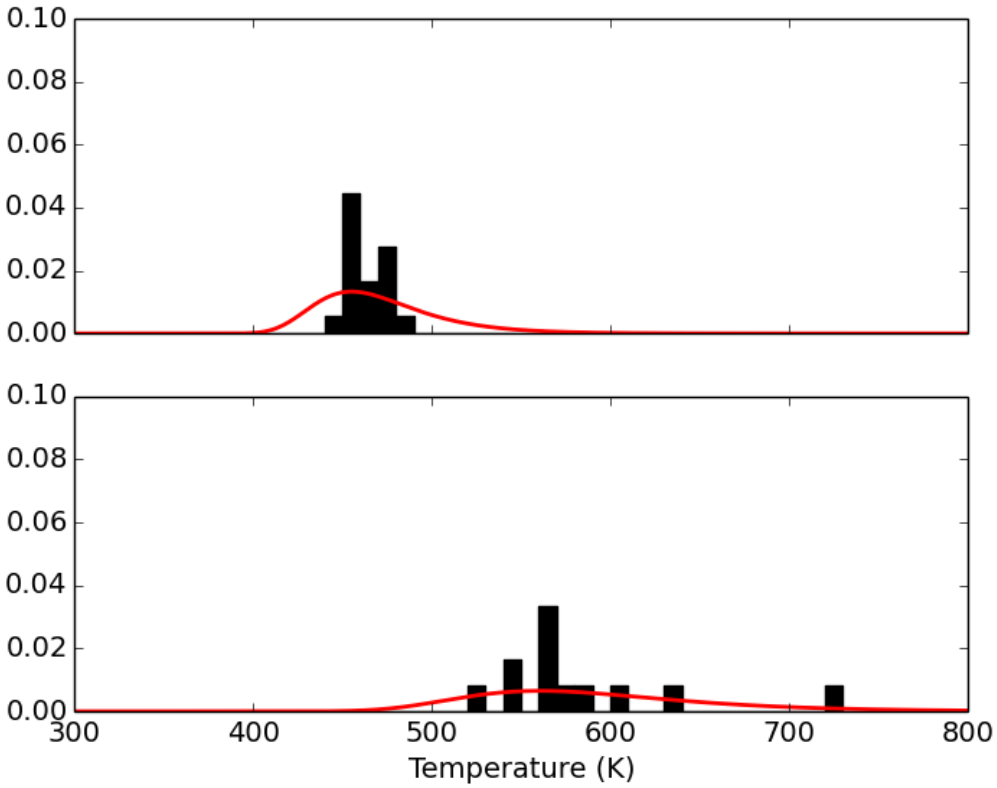

Figure 30: PDFs generated by the linear regression for the mean and shape parameters for the $150\,\mathrm{m\,s^{-1}}$ (top) and $250\,\mathrm{m\,s^{-1}}$ (bottom) cases.

CHAPTER V

CONCLUSIONS AND FUTURE WORK

5.1 Conclusions

The large quantity of energy stored in energetic materials necessitates an understanding of the sensitivity and performance of the material. Computational models for energetic materials offer a safe and cost effective method to explore the fundamental processes of deflagration and detonation in heterogeneous energetic materials. These processes are very difficult to study and require analysis from micro-scales through to macro-scales. Six key capabilities are identified for computational models:

1. Explicit tracking of surface regression due to pyrolysis and surface deformation due to impact loading.

2. Formation of discontinuities such as cracks and plasticizer debonding at arbitrary locations and times not known *a priori*;

3. Ability to model viscoelastic and viscoplastic materials;

4. Inclusion of finite-rate chemical kinetics;

5. Resolution of physical processes at scales approaching the micrometer length scales typical of hotspot formation and energetic crystal sizes;

6. Resolution of macro-scale physical processes such as global burn rates and macro-scale surface deformation.

Numerous computational models are used to simulate energetic materials and these were summarized in Chapter 1. Atomistic approaches are limited by the expense in scaling up their simulation domains to domains of practical interest. The

continuum models using traditional finite volume, finite difference, or finite element approaches all rely on the differential form of the governing equations and require special treatment in the neighborhood of discontinuities in the material such as cracks or material interfaces. Computational models based on an integral form of the governing equations, or the peridynamic theory, avoid the complications around discontinuities because integrals are well-defined over discontinuous fields.

In this work, and existing computational model intended to study the erosion of industrial materials has been extended to study energetic materials. The original Micro-Scale Dynamical Model (MSDM) met all but two of the desired capabilities. The addition of an energy equation enables the MSDM to meet these requirements.

The resulting thermo-mechanical formulation was presented in Chapter 2. The formulation has been shown to fit within the *bond-based* peridynamic framework [55]. This framework has been shown by others to converge to both classical theories of structural mechanics [57] and to molecular dynamics [37, 52]. The MSDM approach has been validated using a variety of temporal schemes and classical problems from structural mechanics.

Surface pyrolysis of heterogeneous solid propellants represents the first of two key applications in this work. Combustion instability in macro-scale rocket motors is influenced by the micro-scale surface details of the propellant. Chapter 3 presented the surface pyrolysis of a randomly packed AP-HTPB propellant with and without catalytic nanoparticle impregnation under a range of operating conditions typically encountered in solid rocket motors. This range corresponds to the upper end of the first and the entirety of the second regimes based on ambient pressure identified by Boggs [12]. At the beginning of the range, the surface regression is primarily planar with little variation in the surface. As the pressure increases, the surface regression appears to be planar from a macro-scale view but ridges and valleys begin to appear at a micro-scale level. As the pressure increases to the end of the simulated

range, the ridges and valleys become sharper and more needle-like. These qualitative observations match those described by Boggs [12]. Comparisons of the MSDM global regression rate to experiments and to recent extensions of the BDP flame model show excellent quantitative agreement with and without catalytic nanoparticles.

The second application investigates the localized heating of a polymer-bound explosive under impact. Regions of localized heating called hotspots form within the material and the structure and location of these hotspots depends on the properties of the binder material and the energetic crystal used. In this work, three common energetics (RDX, HMX, and PETN) as well as a novel energetic (TKX-50) are randomly packed in an Estane binder. This sample undergoes impact against a perfectly rigid surface at a variety of impact speeds from $50\,\mathrm{m\,s^{-1}}$ to $250\,\mathrm{m\,s^{-1}}$.

The results of the simulations indicate that the location of the hotspot is primarily dependent on the properties of the energetic crystal. PETN has a Young's modulus significantly lower than the other materials used resulting in hotspots forming within the energetic crystal itself. The compression of the crystal reduces the energy contained in the wave transmitted into the binder material and no hotspots are formed in the binder itself. RDX and HMX have comparable Young's moduli and transmit the compression wave into the binder with little compression occurring in the energetic crystal itself. This increased energy transmission results in hotspots localized to the binder material between crystals. TKX-50 is unique in the materials simulated. The Young's modulus is significantly larger than RDX and HMX resulting in efficient wave transmission into the binder material. This creates hotspots within the binder between crystals. However, the bulk modulus is also significantly larger, resulting in considerably more heating from small volume changes due to compression. Therefore hotspots also form within the TKX-50 crystal similar to those that formed in PETN crystals.

The impact velocity also plays a strong role in the hotspot location and structure. For the materials in which hotspots form within the binder, whether a hotspot will form between two crystals depends on the spatial separation of the crystals. As the impact velocity increases, the gap sufficient to generate a hotspot also increases. This maximum gap appears to be independent of the energetic crystal properties and dependent on the binder properties; however, an insufficient number of simulations were performed to establish a relationship between the gap size, the impact velocity, and the binder properties. Variations in the binder properties may enhance the hotspot intensity and size or may eliminate the hotspots entirely. Reducing the binder density by a factor of two eliminated the hotspots, consistent with the conclusions reached for a highly shocked, non-planar interface [2].

Lastly, statistical models for the hotspot peak temperature were determined for RDX and HMX. The hotspot structure in these two energetics were virtually indistinguishable due to the mechanical similarities. The hotspot information extracted from both materials led to a dataset robust enough for statistical analysis. The hotspot peak temperature for 3 of the 5 impact velocities were used to generate statistical distributions while the other 2 were retained as control datasets to evaluate the results. The parameters were determined for each impact velocity using maximum-likelihood estimation. The result was the two-parameter Gumbel distribution, a specialization of the Generalized Extreme Value distribution used to model the tails of normally or exponentially distributed variables. A regression between each of the two parameters, the mean and the shape, with impact velocity provided a linear function in velocity for each.

These linear functions were then used to determine the distribution for the control datasets, the hotspot peak temperatures from the $150\,\mathrm{m\,s^{-1}}$ and $250\,\mathrm{m\,s^{-1}}$ cases. These controls provide a means to evaluate the regression when used for interpolation as well as extrapolation. The Kolmogorov-Smirnov test indicated that the validity of

the linear regression to generate statistical models for hotspots may not be rejected. The resulting regressions enable the generation of a physically-accurate hotspot field in macro-scale simulations where the exact processes leading to the hotspot formation may not be adequately resolved.

5.2 Criticisms

Computational modeling always requires the specifications of inputs. Material properties such as density, elastic moduli, thermal moduli and coefficients, and plastic properties are required for continuum simulations regardless of the approach taken. For classical materials (metals, rubbers, etc.), these properties are available from a variety of sources. Experiments frequently measure tensile and compressive properties, thermal responses, and the myriad of other information useful for simulations of these materials. Theoretical and computational tools based on first principles such as molecular dynamics (although the inputs needed for MD are just as numerous and require either theory or experiments as well) can also provide the needed inputs for continuum simulations. Unfortunately, for energetic materials, the options are more limited.

Experimental measurements for energetic materials is quite limited. It is impractical and very unsafe to perform tensile or fracture tests on pure energetic crystals to determine the mechanical properties. Mechanical tests on PBXs and solid propellants may be performed, but this is limited to the combined properties of the mixture and does not provide the properties of the constituents (for example [13,48,49]). This limits the determination of the required properties to theoretical or molecular dynamics approaches.

Unfortunately, some constitutive models require empirical models to account for strain rate and temperature changes. Examples include the viscoelastic Prony series [47] and the Johnson-Cook flow stress model [31]. Many simulations would be

required to generate the requisite information across a range of strain rates and temperatures. Unfortunately, the length and time scale limitations of molecular dynamics simulations limit their usefulness at lower strain rates, compromising their ability to determine accurate values for the model constants.

At its core, the MSDM approach adds an additional complication. One must determine spring and damper coefficients that accurately model the (visco)elastic and (visco)plastic properties of the materials. The majority of the work on mass-spring models in computer graphics relies on the practitioner to specify the spring constants. The increased use of these models for applications requiring quantitative comparison with physical systems has led to attempts to correlate the spring constants to mechanical properties. In the original MSDM formulation extended and evaluated in this work, the structural spring constant was the Young's Modulus, E, of the material while shear and bending springs were omitted [40]. No method to account for Poisson's ratio is available either.

Van Gelder [22] introduced a method to determine the spring constants for a triangular mesh based on the Young's Modulus and the Poisson's ratio, ν. The results indicated convergence to the correct answer in the limit as $\nu \to 0$. For $\nu \neq 0$, Van Gelder's method generates large errors [10, 45]. Baudet *et al* applied a method similar to that of Van Gelder to fully-connected quadrilateral elements [10]. To find the relationship between the spring constants and the elastic material properties, the authors construct the Lagrangian for the system of springs and apply the principle of least action to obtain the governing equations.

Additional techniques exist to determine the spring constants. Spring constants may be determined numerically by comparing a mass-spring system to the appearance of experiments or finite element simulations [43]. Alternatively, the constants may be determined analytically by comparing the mass-spring element with comparable

elements used in finite element methods. Natsupakpong and Çavuşoğlu [45] generate analytical expressions for the spring constants and compare it to the analytical expressions derived by Lloyd *et al.* [43] and Baudet *et al.* [10].

The simplicity of the MSDM concept is offset by the need to establish spring and damper coefficients as well as yield and fracture stresses based on material properties. For explosives, particularly novel explosives, this information may be difficult to generate and there must be collaboration with theoretical, experimental, and molecular dynamics practitioners to generate usable information.

Lastly, all of the work done herein is two-dimensional. This is consistent with the existing literature for the problems studied; however, it is well known that the energetic crystals are anisotropic and their material properties are heterogeneous [51]. Although consistent with the literature, two-dimensional simulations have limited capability to represent the true mechanisms of deformation in the actual materials and additional studies need to be performed to assess the differences.

5.3 Future Work

MSDM has been established as a method suitable for studying the surface pyrolysis in solid propellants and the heating due to impact in PBXs at impact velocities generating elastic compression waves. The final steps in completing the structural model are:

- Inclusion of finite-rate chemical kinetics. The extensions developed during this work permit the inclusion but stopped short of adding them.

- Inclusion of advanced methods to determine spring constants and strain-rate dependent material properties. As discussed in the previous section, the original MSDM formulation used very simple definitions for the spring constants and did not consider strain-rate effects on the yield and fracture stresses. Advanced models have been developed in other communities for spring coefficients

based on material properties and the addition of these models within MSDM will allow a wider range of problems to be considered [45]. The inclusion of Baudet's model [10] will turn MSDM into a *state-based* peridynamic model and will account for arbitrary Poisson's ratio and permit the use of advanced viscoelastic models. Viscoplastic models will account for high-strain-rate and high-temperature effects that are expected to occur during a transition to detonation or surface burning event.

Lastly, both problems (but the surface burning problem in particular) are multiphase in nature and include interactions with the gaseous phase. The result of the chemical reactions during both detonation and deflagration is a large release of high-temperature gaseous products. The tight coupling of the MSDM approach to a fluid solver will enable a detailed study of the interactions between the two phases. This coupling is required to determine the flame standoff height above the heterogeneous propellant, which determines the surface temperature and the subsequent pyrolysis rates and surface structure. This work showed that MSDM is capable of capturing the surface structure when provided the information needed from a fluid solver.

REFERENCES

[1] An, Q., Goddard III, W. A., Zybin, S. V., Jaramillo-Botero, A., and Zhou, T., "Highly shocked polymer bonded explosives at a nonplanar interface: Hot-spot formation leading to detonation," *The Journal of Physical Chemistry C*, vol. 117, no. 50, pp. 26551–26561, 2013.

[2] An, Q., Zybin, S. V., Goddard III, W. A., Jaramillo-Botero, A., Blanco, M., and Luo, S.-N., "Elucidation of the dynamics for hot-spot initiation at nonuniform interfaces of highly shocked materials," *Physical Review B*, vol. 84, no. 22, p. 220101, 2011.

[3] Apte, S. and Yang, V., "Unsteady flow evolution and combustion dynamics of homogeneous solid propellant in a rocket motor," *Combustion and Flame*, vol. 131, no. 1, pp. 110–131, 2002.

[4] Apte, S. and Yang, V., "A large-eddy simulation study of transition and flow instability in a porous-walled chamber with mass injection," *Journal of Fluid Mechanics*, vol. 477, pp. 215–225, 2003.

[5] Baraff, D. and Witkin, A., "Large steps in cloth simulation," in *Proceedings of the 25th annual conference on Computer graphics and interactive techniques*, pp. 43–54, ACM, 1998.

[6] Barua, A., Horie, Y., Kim, S. P., and Zhou, M., "Computational analysis of ignition in heterogeneous energetic materials," in *Materials Science Forum*, vol. 767, pp. 13–21, Trans Tech Publ, 2014.

[7] Barua, A. and Zhou, M., "A Lagrangian framework for analyzing microstructural level response of polymer-bonded explosives," *Modelling and Simulation in Materials Science and Engineering*, vol. 19, no. 5, p. 055001, 2011.

[8] Barua, A. and Zhou, M., "Computational analysis of temperature rises in microstructures of HMX-Estane PBXs," *Computational Mechanics*, pp. 1–9, 2012.

[9] Batcho, P. F. and Schlick, T., "Special stability advantages of position-verlet over velocity-verlet in multiple-time step integration," *The Journal of Chemical Physics*, vol. 115, no. 9, pp. 4019–4029, 2001.

[10] Baudet, V., Beuve, M., Jaillet, F., Shariat, B., and Zara, F., "Integrating Tensile Parameters in Hexahedral Mass-Spring System for Simulation," in *International Conference on Computer Graphics, Visualization and Computer Vision'2009 - WSCG'2009*, Feb. 2009.

[11] Beckstead, M. W., Derr, R., and Price, C., "A model of composite solid-propellant combustion based on multiple flames," *AiAA Journal*, vol. 8, no. 12, pp. 2200–2207, 1970.

[12] Boggs, T., "Deflagration rate, surface structure, and subsurface profile of self-deflagrating single crystals of ammonium perchlorate," *AIAA Journal*, vol. 8, no. 5, pp. 867–873, 1970.

[13] Chen, P., Xie, H., Huang, F., Huang, T., and Ding, Y., "Deformation and failure of polymer bonded explosives under diametric compression test," *Polymer testing*, vol. 25, no. 3, pp. 333–341, 2006.

[14] Chen, Q. and Li, D., "Computer simulation of solid particle erosion," *Wear*, vol. 254, no. 34, pp. 203 – 210, 2003.

[15] Chen, Q. and Li, D., "Computer simulation of erosioncorrosion of a non-passive alloy using a micro-scale dynamic model," *Materials Science and Engineering: A*, vol. 369, no. 12, pp. 284 – 293, 2004.

[16] Cohen, N. S. and Strand, L., "An improved model for the combustion of ap composite propellants," *AIAA Journal*, vol. 20, no. 12, pp. 1739–1746, 1982.

[17] Delingette, H., "Biquadratic and quadratic springs for modeling St Venant Kirchhoff materials," in *Proceedings of the 4th international symposium on Biomedical Simulation*, no. 4 in ISBMS '08, (Berlin, Heidelberg), pp. 40–48, Springer-Verlag, 2008.

[18] Demmie, P. N. and Silling, S. A., "An approach to modeling extreme loading of structures using peridynamics," *Journal of Mechanics of Materials and Structures*, vol. 2, no. 10, pp. 1921–1945, 2007.

[19] Efron, B. and Tibshirani, R., "Bootstrap methods for standard errors, confidence intervals, and other measures of statistical accuracy," *Statistical science*, pp. 54–75, 1986.

[20] Findley, W. N. and Davis, F., *Creep and relaxation of nonlinear viscoelastic materials*. Courier Dover Publications, 2011.

[21] Frazier, C., Demko, A. R., and Petersen, E. L., "Modeling composite solid propellant with catalytic additives," *51st AIAA Aerospace Sciences Meeting*, vol. AIAA 2013-0820, 2013.

[22] Gelder, A. V., "Approximate simulation of elastic membranes by triangulated spring meshes," *Journal of graphics tools*, vol. 3, no. 2, pp. 21–41, 1998.

[23] Gilbert, J., Chakravarthy, S., and Gonthier, K. A., "Computational analysis of hot-spot formation by quasi-steady deformation waves in porous explosive," *Journal of Applied Physics*, vol. 113, no. 19, pp. –, 2013.

[24] Goddard, W. personal communication.

[25] Groot, R. D. and Warren, P. B., "Dissipative particle dynamics: Bridging the gap between atomistic and mesoscopic simulation," *The Journal of Chemical Physics*, vol. 107, no. 11, pp. 4423–4435, 1997.

[26] Gumbel, E. J. and Lieblein, J., *Statistical theory of extreme values and some practical applications: a series of lectures*, vol. 33. US Government Printing Office Washington, 1954.

[27] Hamate, Y. and Horie, Y., "Ignition and detonation of solid explosives: a micromechanical burn model," *Shock Waves*, vol. 16, no. 2, pp. 125–147, 2006.

[28] Hooper, J. B., Bedrov, D., Smith, G. D., Hanson, B., Borodin, O., Dattelbaum, D. M., and Kober, E. M., "A molecular dynamics simulation study of the pressure-volume-temperature behavior of polymers under high pressure," *The Journal of Chemical Physics*, vol. 130, no. 14, pp. –, 2009.

[29] Hu, J., Li, D., and Llewellyn, R., "Synergistic effects of microstructure and abrasion condition on abrasive wear of composites – a modeling study," *Wear*, vol. 263, no. 16, pp. 218 – 227, 2007. 16th International Conference on Wear of Materials.

[30] Jacobs, P. W. M. and Whitehead, H., "Decomposition and combustion of ammonium perchlorate," *Chemical Reviews*, vol. 69, no. 4, pp. 551–590, 1969.

[31] Johnson, G. R. and Cook, W. H., "A constitutive model and data for metals subjected to large strains, high strain rates and high temperatures," in *Proceedings of the 7th International Symposium on Ballistics*, vol. 21, pp. 541–547, The Netherlands, 1983.

[32] Jones, E., Oliphant, T., Peterson, P., and others, "SciPy: Open source scientific tools for Python," 2001–. [Online; accessed 2014-09-19].

[33] Jung, T. and Yoh, J. J., "Model for melt-layer front in Ammonium Perchlorate propellant combustion," *Journal of propulsion and power*, vol. 26, no. 5, pp. 993–997, 2010.

[34] Kim, K.-H. and Yoh, J. J., "A particle level-set based eulerian method for multi-material detonation simulation of high explosive and metal confinements," *Proceedings of the Combustion Institute*, vol. 34, no. 2, pp. 2025 – 2033, 2013.

[35] Knott, G., Jackson, T., and Buckmaster, J., "Random packing of heterogeneous propellants," *AIAA Journal*, vol. 39, no. 4, pp. 678–686, 2001.

[36] Kubota, S., Saburi, T., Ogata, Y., and Nagayama, K., "Numerical simulation of detonation propagation in PETN at arbitrary intitial density by simple model," in *AIP Conference Proceedings*, vol. 1426, p. 231, 2012.

[37] Lehoucq, R. B. and Silling, S. A., "Statistical coarse-graining of molecular dynamics into peridynamics," *Report SAND2007-6410, Sandia National Laboratories, Albuquerque, New Mexico*, 2007.

[38] Li, D., Chen, Q., and Cook, B., "A further simulation study on the dual role of porosity in solid-particle erosion of materials," *Wear*, vol. 271, no. 9, pp. 1325–1330, 2011.

[39] Li, D., Elalem, K., Anderson, M., and Chiovelli, S., "A microscale dynamical model for wear simulation," *Wear*, vol. 225229, Part 1, no. 0, pp. 380 – 386, 1999.

[40] Li, L. and Li, D., "Simulation of corrosion-erosion of passive metals using a micro-scale dynamical model," *Wear*, vol. 271, no. 910, pp. 1404 – 1410, 2011. 18th International Conference on Wear of Materials.

[41] Littell, R. C., Mc Clave, J. T., and Offen, W. W., "Goodness-of-fit tests for the two parameter weibull distribution," *Communications in Statistics - Simulation and Computation*, vol. 8, no. 3, pp. 257–269, 1979.

[42] Liu, M. and Liu, G., "Smoothed particle hydrodynamics (SPH): an overview and recent developments," *Archives of Computational Methods in Engineering*, vol. 16, no. 1, pp. 25–76, 2010.

[43] Lloyd, B. A., Székely, G., and Harders, M., "Identification of spring parameters for deformable object simulation," *Visualization and Computer Graphics, IEEE Transactions on*, vol. 13, no. 5, pp. 1081–1094, 2007.

[44] Maillet, J. B., Bourasseau, E., Desbiens, N., Vallverdu, G., and Stoltz, G., "Mesoscopic simulations of shock-to-detonation transition in reactive liquid high explosive," *EPL (Europhysics Letters)*, vol. 96, no. 6, p. 68007, 2011.

[45] Natsupakpong, S. and Cenk Çavuşoğlu, M., "Determination of elasticity parameters in lumped element (mass-spring) models of deformable objects," *Graphical Models*, vol. 72, no. 6, pp. 61–73, 2010.

[46] Olinger, B., Halleck, P. M., and Cady, H. H., "The isothermal linear and volume compression of pentaerythritol tetranitrate (PETN) to 10 GPa (100 kbar) and the calculated shock compression," *The Journal of Chemical Physics*, vol. 62, no. 11, 1975.

[47] Park, S. and Schapery, R., "Methods of interconversion between linear viscoelastic material functions. part ia numerical method based on prony series," *International Journal of Solids and Structures*, vol. 36, no. 11, pp. 1653 – 1675, 1999.

[48] Rae, P., Goldrein, H., Palmer, S., Field, J., and Lewis, A., "Quasi–static studies of the deformation and failure of β–hmx based polymer bonded explosives," *Proceedings of the Royal Society of London. Series A: Mathematical, Physical and Engineering Sciences*, vol. 458, no. 2019, pp. 743–762, 2002.

[49] Rae, P., Palmer, S., Goldrein, H., Field, J., and Lewis, A., "Quasi–static studies of the deformation and failure of pbx 9501," *Proceedings of the Royal Society of London. Series A: Mathematical, Physical and Engineering Sciences*, vol. 458, no. 2025, pp. 2227–2242, 2002.

[50] Ramaswamy, A. L., "Mesoscopic approach to energetic material sensitivity," *Journal of Energetic Materials*, vol. 24, no. 1, pp. 35–65, 2006.

[51] Rimoli, J., Gürses, E., and Ortiz, M., "Shock-induced subgrain microstructures as possible homogenous sources of hot spots and initiation sites in energetic polycrystals," *Physical Review B*, vol. 81, no. 1, p. 014112, 2010.

[52] Seleson, P., Parks, M. L., Gunzburger, M., and Lehoucq, R. B., "Peridynamics as an upscaling of molecular dynamics," *Multiscale Modeling & Simulation*, vol. 8, no. 1, pp. 204–227, 2009.

[53] Sewell, T. D. and Bennett, C. M., "Monte Carlo calculations of the elastic moduli and pressure-volume-temperature equation of state for hexahydro-1,3,5-trinitro-1,3,5-triazine," *Journal of Applied Physics*, vol. 88, no. 1, pp. 88–95, 2000.

[54] Sewell, T. D., Menikoff, R., Bedrov, D., and Smith, G. D., "A molecular dynamics simulation study of elastic properties of HMX," *The Journal of Chemical Physics*, vol. 119, no. 14, pp. 7417–7426, 2003.

[55] Silling, S., "Reformulation of elasticity theory for discontinuities and long-range forces," *Journal of the Mechanics and Physics of Solids*, vol. 48, no. 1, pp. 175 – 209, 2000.

[56] Silling, S., Epton, M., Weckner, O., Xu, J., and Askari, E., "Peridynamic states and constitutive modeling," *Journal of Elasticity*, vol. 88, no. 2, pp. 151–184, 2007.

[57] Silling, S. A. and Lehoucq, R. B., "Convergence of peridynamics to classical elasticity theory," *Journal of Elasticity*, vol. 93, no. 1, pp. 13–37, 2008.

[58] Tran, L. and Udaykumar, H., "Simulation of void collapse in an energetic material, part 2: reactive case," *Journal of propulsion and power*, vol. 22, no. 5, pp. 959–974, 2006.

[59] Tran, L. and Udaykumar, H., "Simulation of void collapse in an energetic material, part i: Inert case," *Journal of propulsion and power*, vol. 22, no. 5, pp. 947–958, 2006.

[60] Tran, L. and Udaykumar, H., "A particle-level set-based sharp interface cartesian grid method for impact, penetration, and void collapse," *Journal of Computational Physics*, vol. 193, no. 2, pp. 469 – 510, 2004.

[61] Xu, X.-P. and Needleman, A., "Numerical simulations of fast crack growth in brittle solids," *Journal of the Mechanics and Physics of Solids*, vol. 42, no. 9, pp. 1397 – 1434, 1994.

[62] Zaoui, A. and Sekkal, W., "Molecular dynamics study of mechanical and thermodynamic properties of pentaerythritol tetranitrate," *Solid State Communications*, vol. 118, no. 7, pp. 345 – 350, 2001.

[63] Zhang, J., Jackson, T. L., Buckmaster, J. D., and Freund, J. B., "Numerical modeling of shock-to-detonation transition in energetic materials," *Combustion and Flame*, vol. 159, no. 4, pp. 1769–1778, 2012.

[64] Zhang, R., Zhang, M., and Shu, C.-W., "On the order of accuracy and numerical performance of two classes of finite volume weno schemes," *Communications in Computational Physics*, vol. 9, pp. 807–827, March 2011.